

Global identification of solid waste methane super emitters using hyperspectral satellites

Xin Zhang^{a,1}, Joannes D. Maasackers^a, Javier Roger^b, Luis Guanter^{b,c}, Shubham Sharma^a, Srijana Lama^a, Paul Tol^a, Daniel J. Varon^d, Daniel H. Cusworth^e, Katherine Howell^e, Andrew K. Thorpe^f, Philip G. Brodrick^f, and Ilse Aben^{a,g}

^aSRON Netherlands Institute for Space Research, 2333 CA Leiden, The Netherlands;

^bResearch Institute of Water and Environmental Engineering, Universitat Politècnica de València, Valencia 46022, Spain;

^cEnvironmental Defense Fund, 1083 HN Amsterdam, The Netherlands;

^dSchool of Engineering and Applied Sciences, Harvard University, Cambridge, MA 02138;

^eCarbon Mapper, Pasadena, CA 91105;

^fJet Propulsion Laboratory, California Institute of Technology, Pasadena, CA 91109;

^gDepartment of Earth Sciences, Vrije Universiteit Amsterdam, 1081 HV Amsterdam, The Netherlands

¹To whom correspondence should be addressed. Email: xin.zhang@sron.nl

This is a non-peer-reviewed preprint submitted to EarthArXiv.



Global Identification of Solid Waste Methane Super Emitters using Hyperspectral Satellites

Xin Zhang,^{*,†} Joannes D. Maasackers,[†] Javier Roger,[‡] Luis Guanter,^{‡,¶} Shubham Sharma,[†] Srijana Lama,[†] Paul Tol,[†] Daniel J. Varon,[§] Daniel H. Cusworth,^{||} Katherine Howell,^{||} Andrew K. Thorpe,[⊥] Philip G. Brodrick,[⊥] and Ilse Aben^{†,#}

[†]*SRON Netherlands Institute for Space Research, Leiden, 2333 CA, The Netherlands*

[‡]*Research Institute of Water and Environmental Engineering, Universitat Politècnica de València, Valencia 46022, Spain*

[¶]*Environmental Defense Fund, Amsterdam, 1083 HN, The Netherlands*

[§]*School of Engineering and Applied Sciences, Harvard University, Cambridge, 02138, MA, USA*

^{||}*Carbon Mapper, Pasadena, 91105, CA, USA*

[⊥]*Jet Propulsion Laboratory, California Institute of Technology, Pasadena, 91109, CA, USA*

[#]*Department of Earth Sciences, Vrije Universiteit Amsterdam, Amsterdam, 1081 HV, The Netherlands*

E-mail: xin.zhang@sron.nl

Abstract

Solid waste is the third largest source of anthropogenic methane and mitigating emissions is crucial for addressing climate change. We combine three high-resolution (30–60 m) hyperspectral satellite imagers (EMIT, EnMAP, and PRISMA) to quantify

emissions from 38 strongly-emitting disposal sites across worldwide urban methane hotspots. The imagers give consistent emission estimates, with EMIT and EnMAP having better sensitivity than PRISMA. Total observed emissions add up to $230 \pm 15 \text{ t h}^{-1}$, representing 5% of reported global solid waste emissions. Our estimates exceed the facility-level Climate TRACE inventory by a factor of 1.8, while we only detect emissions from 9 of the inventory’s 20 highest-emitting sites, highlighting the importance of facility-level information. Furthermore, multi-month observations reveal emission patterns potentially linked to facility operations. We estimate that these instruments could detect up to 60% of global landfill emissions, critically expanding on satellite instruments designed for methane and supporting emission mitigation.

Keywords

methane, hyperspectral, landfill, satellite, remote sensing

Synopsis

Landfills and dumping sites are major sources of methane emissions driving climate change. New hyperspectral satellite imagers reveal higher emissions than previously known, improving global emission monitoring capabilities.

Introduction

Methane is a potent greenhouse gas with a global warming potential 27–30 times higher than carbon dioxide over a 100-year time scale.¹ Its relatively short atmospheric lifetime of about a decade makes reducing methane emissions critical for mitigating near-term global warming. Anthropogenic activities account for $\sim 60\%$ of global methane emissions, with waste treatment as the third largest source (18%) after agriculture and fossil fuel exploitation.²

Moreover, the global waste generation could increase by $\sim 60\%$ from 2016 to 2050,³ Waste methane emission reductions have become a priority for global climate action, as exemplified by the ‘Declaration on Reducing Methane from Organic Waste’ declaration introduced at the 29th UN Climate Change Conference (COP29).⁴ In this declaration, countries responsible for over 50% of organic waste methane emissions committed to including reduction strategies in their climate plans. Several countries already announced specific plans and the Lowering Organic Waste Methane (LOW-Methane) initiative is focused on reducing annual global waste methane emissions by one million metric tonnes a year by 2030 and unlocking 10 billion dollars in funding to achieve this goal.⁵

However, accurately quantifying landfill methane emissions remains challenging, with substantial uncertainties in both site-specific and global estimates.⁶⁻⁹ While traditional approaches rely on modeling and limited aircraft measurements,^{6,10-13} space-borne monitoring offers a way to improve emission quantification. A 2022 study¹⁴ demonstrated the application of GHGSat observations to quantify emissions from four landfills, including one in Buenos Aires that contributed 50% of the city’s methane emissions. However, facility-scale coverage by satellites designed to observe methane is currently limited. Here we therefore evaluate the potential of using alternative imaging spectrometers to extend that coverage and quantify emissions from individual landfills.

The TROPOspheric Monitoring Instrument (TROPOMI)^{15,16} has been used for monitoring regional methane emissions^{17,18} and detecting urban super-emitters.^{14,19} However, its spatial resolution ($5.5 \times 7 \text{ km}^2$ at nadir) typically cannot separate landfill emissions from other city emissions.¹⁴ Currently, the only operational spaceborne instruments specifically designed to measure methane at facility-level are the commercial satellites from the GHGSat constellation.^{20,21} A small fraction of the GHGSat data are publicly available and individual observations only cover an area of $\sim 12 \times 15 \text{ km}^2$. Recent studies highlight the use of public multispectral²²⁻²⁴ and hyperspectral imagers (HSIs)²⁵⁻²⁷ for detecting large point sources, primarily from the oil/gas industry. HSIs, similar to the next generation Airborne

Visible/Infrared Imaging Spectrometer (AVIRIS-NG),^{8,28} are not designed for methane detection but offer relatively high methane sensitivity through hundreds of narrow spectral bands. Starting with PRecurso IperSpettrale della Missione Applicativa (PRISMA),^{29,30} HSIs have been verified to be capable of detecting plumes down to 300–500 kg h⁻¹^{31,32} in favorable conditions such as bright homogeneous desert scenes, outperforming multispectral sensors such as Sentinel-2.^{22–24} Thus, HSIs are particularly promising for detecting landfill methane emissions, which are more diffuse than those from oil/gas operations and occur over more complex terrain.

Previous studies have demonstrated the potential of HSIs in detecting landfill methane emissions. The Environmental Mapping and Analysis Program (EnMAP)^{33,34} has been used to detect emissions from the Ghazipur and Okhla landfills in Delhi,²⁷ while Earth Surface Mineral Dust Source Investigation (EMIT)^{33,34} has been used to detect emissions from 11 different landfills around the world.²⁶ To assist in mitigating global landfills, it is crucial to construct a comprehensive global landfill emission dataset. Here, we integrate TROPOMI and three HSIs (EMIT, EnMAP, and PRISMA) to identify, quantify, and monitor high-emitting landfills worldwide. As part of the analysis, we compare the performance of all HSIs and examine the impact of wind speed uncertainty on the emission quantification. We also compare our results against existing emission inventories. Our analysis assesses hyperspectral imaging’s potential to monitor global landfill methane, expanding upon current satellite capabilities designed for methane observation.

Results

Landfill Methane Hot Spots

Figure 1 shows the overview of urban and landfill methane hot spots detected by TROPOMI and HSIs, along with examples of typical methane plumes observed by HSIs. Using 2020–2023 TROPOMI data, we identified persistent global urban methane hot spots based on

plume detections and analysis of long-term averages (see *Methods*).^{14,19} Among all hot spots, 58 are potentially associated with landfill emissions given their source locations, although they may also include contributions from other urban sources. We evaluate 46 landfills within these TROPOMI hot spots using EMIT and EnMAP, while the remaining 12 lack observations. PRISMA has clear-sky observations for 49 landfills (Figure S8) but only detects plumes from 4 due to its lower methane sensitivity, caused by lower signal-to-noise ratio (SNR) and spectral resolution (see *Methods*).

Overall, the HSI data reveal detectable plumes from 38 landfills: 25 within 15 km of TROPOMI hot spots and 13 at nearby locations (Figure 1). EMIT, with its wider scene coverage, observes all 38 landfills in clear-sky conditions and detects plumes from 36 (Figure S8). EnMAP shows a comparable capability, detecting plumes from 16 out of 18 observed landfills, while PRISMA, due to its lower sensitivity, only detects plumes at 4 out of 32 observed sites. Among the 38 landfills with detected plumes, 29 are observed at least twice, with 10 having 8–14 plume detections, facilitating emission time series analysis (see *Emission Variations*). The total number of plumes detected by each HSI is as follows: EMIT observes 132 plumes, EnMAP 38, and PRISMA 10 (Figure S9).

This highlights the potential of EMIT and EnMAP in identifying landfill emission sources, whereas PRISMA is constrained by a higher detection threshold. When calculating mean emission rates, we use different approaches for each instrument. For EnMAP and EMIT, we conservatively assume zero emission when clear-sky overpasses yield no detected plumes. In the case of PRISMA, owing to its lower sensitivity, we only include instances where plumes are detected in our emission rate calculations.

Landfill Methane Emission Rates

A commonly used data-driven approach for methane retrieval from HSIs involves a matched filter algorithm that maximizes the signal-to-background ratio by identifying pixels exhibiting the strongest correlation with methane’s absorption spectrum. We improve the traditional

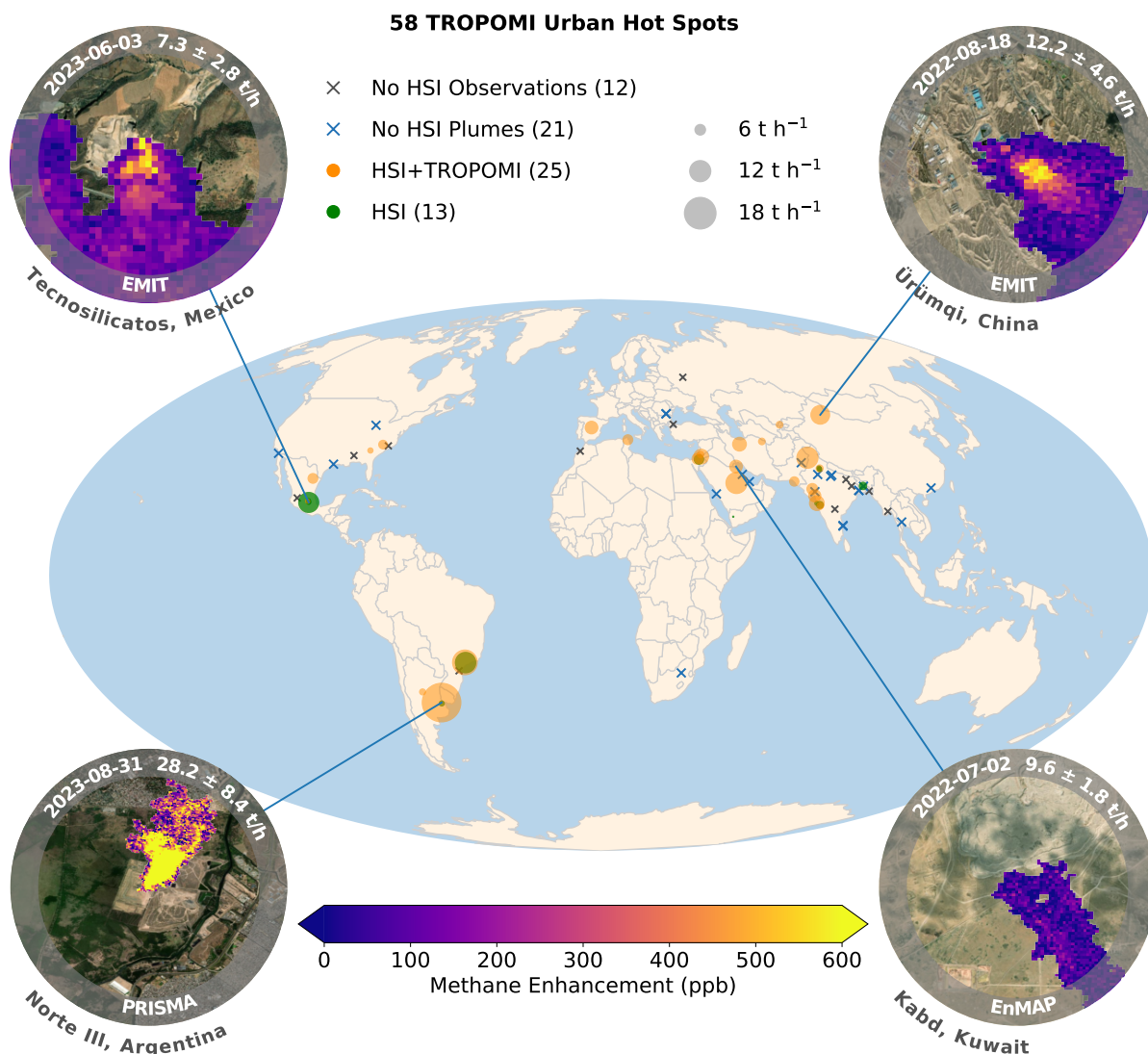


Figure 1: Urban hot spots detected by TROPOMI (2020–2023) and landfill emissions detected at those hot spots using hyperspectral imagers (HSIs) including EMIT, EnMAP, and PRISMA. Gray crosses indicate TROPOMI hot spots without clear-sky HSI data, blue crosses show hot spots with clear-sky HSI observations without detected plumes, orange circles show TROPOMI hot spots with HSI plumes, and green circles indicate plumes detected by HSIs slightly away from the TROPOMI hot spots. The 'No HSI Observations' group excludes PRISMA due to its lower methane sensitivity. Insets show typical landfill plumes with detection date, emission rate, uncertainty, landfill/country name, and instrument. Background imagery comes from Esri World Imagery.³⁵ Figure S7 shows a zoomed-in view of landfill emissions across India.

matched filter to retrieve methane enhancements using Level 1 radiance data and to estimate emission rates through the integrated mass enhancement (IME) method, specifically calibrated for each instrument (see *Methods*). The reported uncertainties include contributions from wind speed error, retrieval random error, and IME calibration error (Supplementary Section S1). We validate our methodology using two controlled releases (Supplementary Section S2), one for PRISMA (October 21, 2021) and one for EnMAP (November 16, 2022). Both controlled releases show our satellite estimates agree with the controlled flow rates within their uncertainties (Figure S2). While these validations are performed using point-source controlled releases, we expect controlled releases simulating more dispersed emissions from landfills will become available in the near-future. While the overpasses for different HSIs typically vary in timing over the same landfill, the average magnitudes of emission rates between EnMAP and EMIT are consistent (slope=1.21±0.17, r=0.84, Figure S10a). We therefore use data from both instruments together for the remainder of this study. PRISMA’s emission rate estimates for two landfills are consistent with those from EMIT and EnMAP in the same year (Figure S10b).

Figure 2 shows our methane emission rates for 38 landfills across 17 countries with the lowest rate being $\sim 1 \text{ t h}^{-1}$. The sum of mean emission rates across sites is $230 \pm 15 \text{ t h}^{-1}$, with most of the observed high-emitting landfills located at hot spots in India, Argentina, Brazil, and Mexico. India stands out with the highest total of $41.4 \pm 5.0 \text{ t h}^{-1}$ from 10 landfills. Argentina follows at $28.1 \pm 6.6 \text{ t h}^{-1}$, primarily driven by the Norte III landfill in Buenos Aires, showing the highest emission rate among all observed landfills at $22.0 \pm 6.4 \text{ t h}^{-1}$. Brazil has a similar emission of $25.6 \pm 6.3 \text{ t h}^{-1}$, with the Caieiras ($14.0 \pm 4.8 \text{ t h}^{-1}$) and Pedreira ($11.5 \pm 4.0 \text{ t h}^{-1}$) landfills in Sao Paulo strongly contributing to this total. These three large-emitting landfills in Buenos Aires and Sao Paulo account for 20% of the total quantified landfill methane emissions. Mexico ranks fourth at $23.7 \pm 5.3 \text{ t h}^{-1}$, half of which comes from the Tecnosilicatos landfill in Mexico City.

Among the remaining 13 countries, each with only 1 to 2 observed landfills, six have a

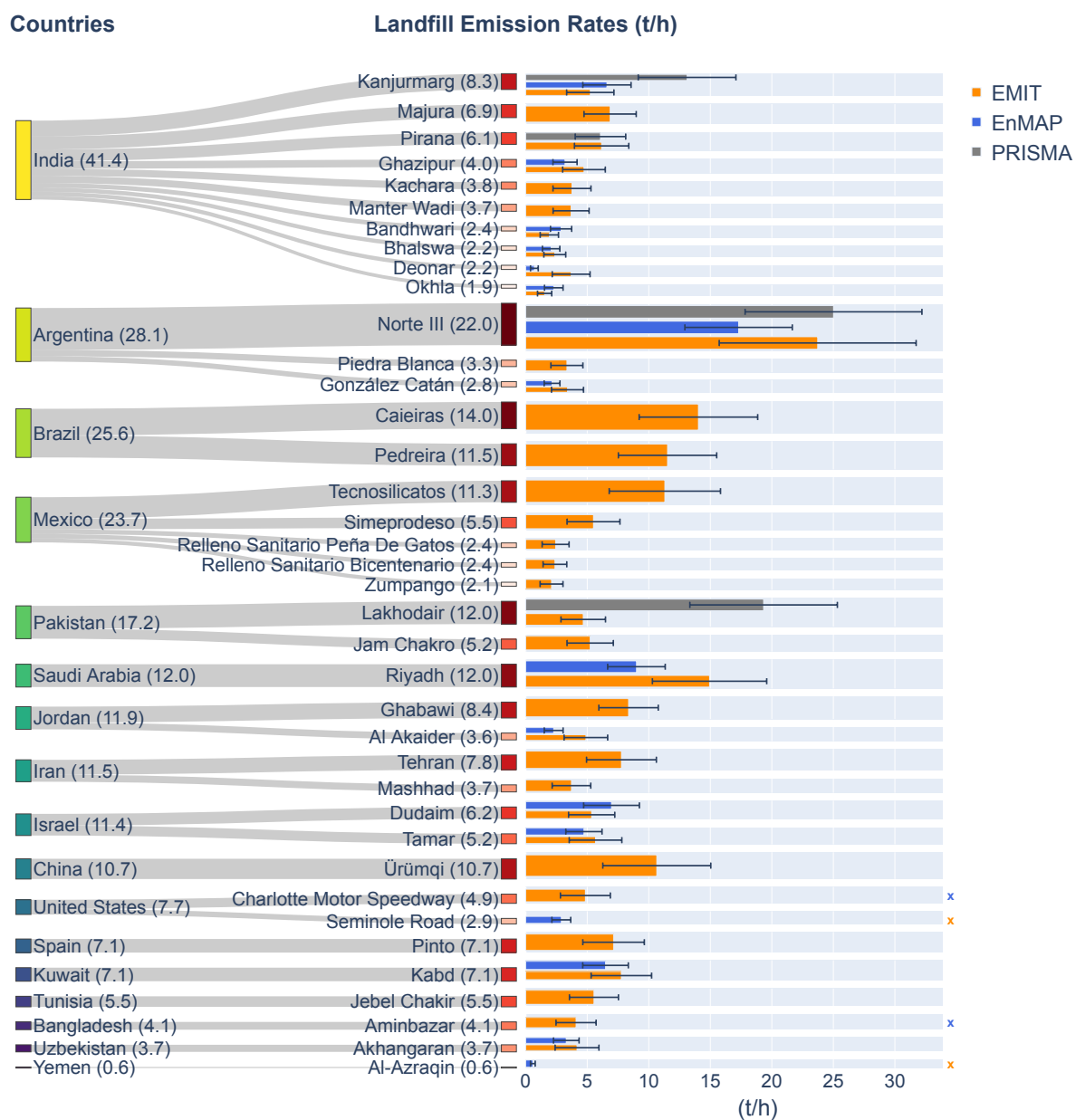


Figure 2: Sankey plot for the landfill emissions estimated using hyperspectral imagers (HSIs). Box heights are proportional to emission rates ($t\ h^{-1}$), with values in brackets. Colored bars show estimates from different instruments, with uncertainties in black. Crosses on the right indicate EMIT or EnMAP overpasses without detected methane plumes. Non-detections with PRISMA are not depicted, given PRISMA's lower sensitivity. More details are given in Tables S1 and S2.

total emission rate ranging from 10 to 17 t h⁻¹. This can be attributed to the presence of large emitting landfills, such as the Lakhodair landfill (12.0 ± 4.2 t h⁻¹) in Pakistan, the Riyadh landfill (12.0 ± 3.4 t h⁻¹) in Saudi Arabia, the Ürümqi landfill (10.7 ± 4.4 t h⁻¹) in China, the Ghabawi landfill (8.4 ± 2.4 t h⁻¹) in Jordan, and the Tehran landfill (7.8 ± 2.8 t h⁻¹) in Iran. The cumulative distribution reveals that for this set of 38 landfills, the top 20% highest emitters contribute 46% of the inferred total emission (Figure S11a). This highlights the importance of detecting and mitigating high methane-emitting landfills. Due to variations in background noise levels, wind speed, and potential methane emission variability, landfill methane plumes are sometimes detected by one HSI and missed by another (crosses in Figure 2). This emphasizes the value of combining multiple HSIs to monitor landfill emissions. However, in most cases, both EnMAP and EMIT detect emissions from specific landfills, thereby increasing the observation opportunities for landfill emissions. For cases with a single detected plume (Figure S9), estimates may be affected by potential offsets. Future studies with more data will be crucial for refining these constraints.

Comparison with Observations and Inventories

First, we compare our HSI estimates with recent satellite, aircraft, and ground-based observations (Figure 3a).^{14,26,36,37} For eight of the observed landfills, there are estimates from earlier studies. Our HSI results show good agreement with these estimates (slope=1.31±0.14, r=0.97, Figure 3a), though the number of data points is limited (Table S3). We then compare our facility-level methane emission estimates with the Climate Tracking Real-time Atmospheric Carbon Emissions (Climate TRACE) dataset, which models emissions using multiple waste datasets (see *Methods*). We find that the Climate TRACE dataset generally underestimates landfill emissions compared to HSI for the 26 landfills with overlapping estimates (Figure 3a and Table S4). Based on the HSI measurements, total methane emissions (141 ± 11 t h⁻¹) from these landfills are 1.8 times higher than the estimates in the Climate TRACE inventory. Some of the data used in the Climate Trace inventory may be outdated.

For example, the Norte III landfill data from the 2013 Waste Atlas reports emissions of 3.3 t h^{-1} , significantly lower than our estimate of $22.0 \pm 6.4 \text{ t h}^{-1}$. Considering only the 2021 and 2022 Climate Trace data for 15 landfills, our estimates are only 1.3 times higher. However, comparing individual facilities, the median ratio between our estimates and the Climate Trace data is still 4.7, exceeding the 1.6 ratio found in comparisons with previous studies. Therefore, the differences appear to be related not only to up-to-date information on landfill activities but also to appropriate emission factors representative of operations at the different landfills.

In addition to the landfills at hot spots, we then focus on Climate TRACE’s top 20 highest emitting landfills (Figure 3b and Table S5). HSIs overpass all 20 landfills, but only detect plumes from 9 still-active landfills, while the remaining 11 appear inactive based on vegetation covering the landfill as seen in Sentinel-2 imagery (Figure S12). Among nine active landfills, our estimates are consistent with Climate TRACE for four but are 48~71% lower for the other five. For two of these landfills (Tehran and Loma Los Colorados), additional observational estimates are available in the literature. Our estimate for the Tehran landfill agrees with an earlier EMIT analysis.²⁶ However, four Airborne Visible InfraRed Imaging Spectrometer – Next Generation (AVIRIS-NG) observations of the Loma Los Colorados landfill in January and February 2023 reported emissions of $1.2 \pm 0.3 \text{ t h}^{-1}$,³⁷ which is 89% lower than our EMIT-based estimate for January and 90% lower than the Climate TRACE estimate. These results show that differences between facility-level observations and bottom-up estimates can go both ways and that there may be substantial temporal variability in emissions. Some variability may also be due to differences in quantification algorithms applied to remote sensing datasets. Using the same EMIT observations, we compare methane emissions across 36 landfills using Carbon Mapper’s IME-fetch method (Supplementary Section S4). We find that some significant variability can be traced to quantification uncertainties, particularly in plume masking. This variability can be reproduced using large-eddy simulations. Despite these variations, the overall emission results remain consistent across quantification

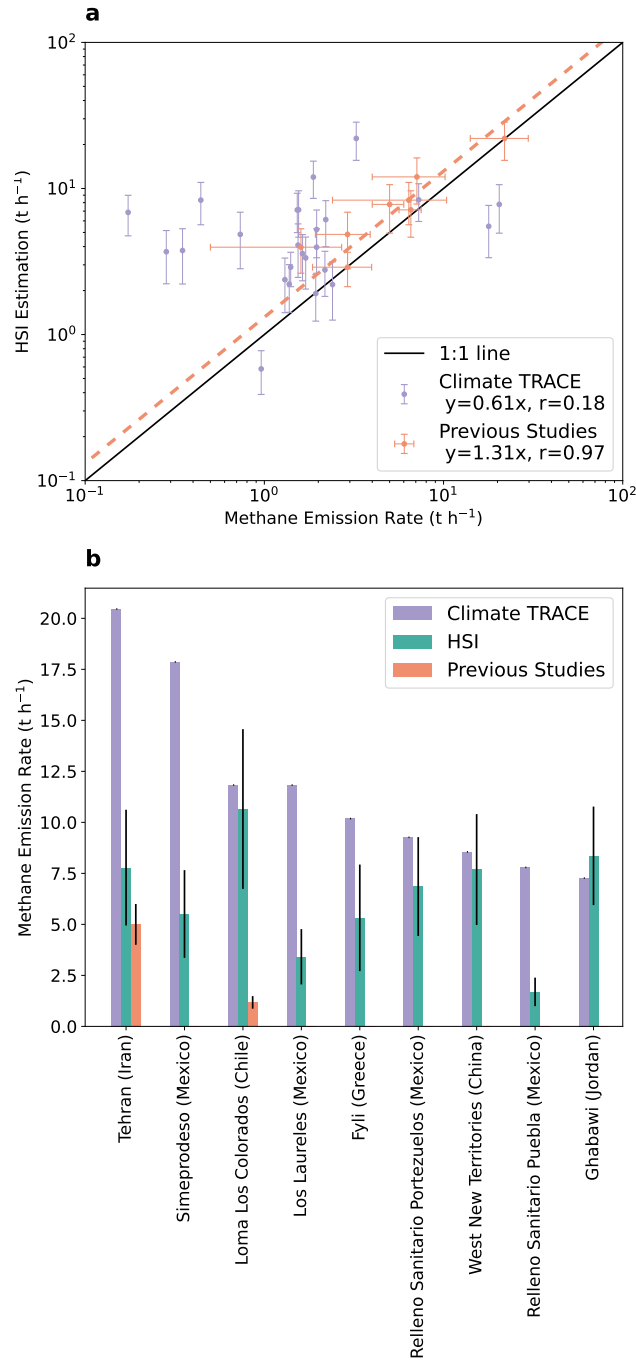


Figure 3: Comparison of methane emission rates from hyperspectral imager (HSI) observations, the Climate TRACE inventory, and observational estimates from the literature for (a) landfills mapped in Figure 1, and (b) the top 20 methane-emitting landfills in the Climate TRACE dataset (see Table S3, S4, and S5 for details). The regression coefficients are calculated using orthogonal distance regression. The Pearson correlation coefficients are 0.18 between HSI and Climate TRACE, and 0.97 between HSI and previous studies.

algorithms for most landfills in this study.

In addition to facility-level comparisons, we evaluate how our HSI estimates compare to solid waste methane emission inventories at the city scale from the Waste Methane Assessment Platform (WasteMAP). Of the 15 cities included in both the WasteMAP platform and our analysis, accounting for uncertainties, only two have higher emissions in WasteMAP than our summed HSI landfill estimates (Figure S13a and Table S6). HSI emissions from the Pinto (Spain), Simeprodeso (Mexico), and Jebel Chakir (Tunisia) landfills alone are 16~27 times higher than total city emissions for Madrid, Monterrey, and Tunis, respectively. The mean ratio of our HSI-derived landfill emissions to city totals is 6.3. One reason for this high ratio may be that these landfills service a larger area than the cities they are within. Meanwhile, this ratio is likely underestimated because emissions from many smaller landfills are undetected by HSI.

At the country level, Climate TRACE solid waste emissions generally exceed the sum of our HSI landfill emissions (Figure S13b and Table S7). This difference arises because HSI measurements typically only cover a small fraction of the landfills included in the Climate TRACE data, while Climate TRACE’s country-level inventory considers all solid waste emissions. However, Climate TRACE’s total facility-level emissions are 47% lower than HSI estimates in six countries, while the remaining countries show emissions that are either higher than or comparable to HSI estimates (Figure S13b). These findings highlight the importance of evaluating and improving emission inventories across scales using observations, particularly accounting for strongly-emitting landfills that may be underestimated in current inventories.

Emission Variations

The multiple overpasses of HSIs enable us to examine the spatial and temporal variations in emissions (Figure S14). Specifically, the Ghabawi landfill in Jordan has a total of 14 EMIT observations, with measurements taken every 1–2 months throughout 2023 (Figure

4). Between February and April 2023, the emission rate increased from $5.1 \pm 1.7 \text{ t h}^{-1}$ to $17.2 \pm 4.3 \text{ t h}^{-1}$. Then it decreased to $3.9 \pm 1.8 \text{ t h}^{-1}$ in September, before increasing again to $9.3 \pm 2.1 \text{ t h}^{-1}$ in December.

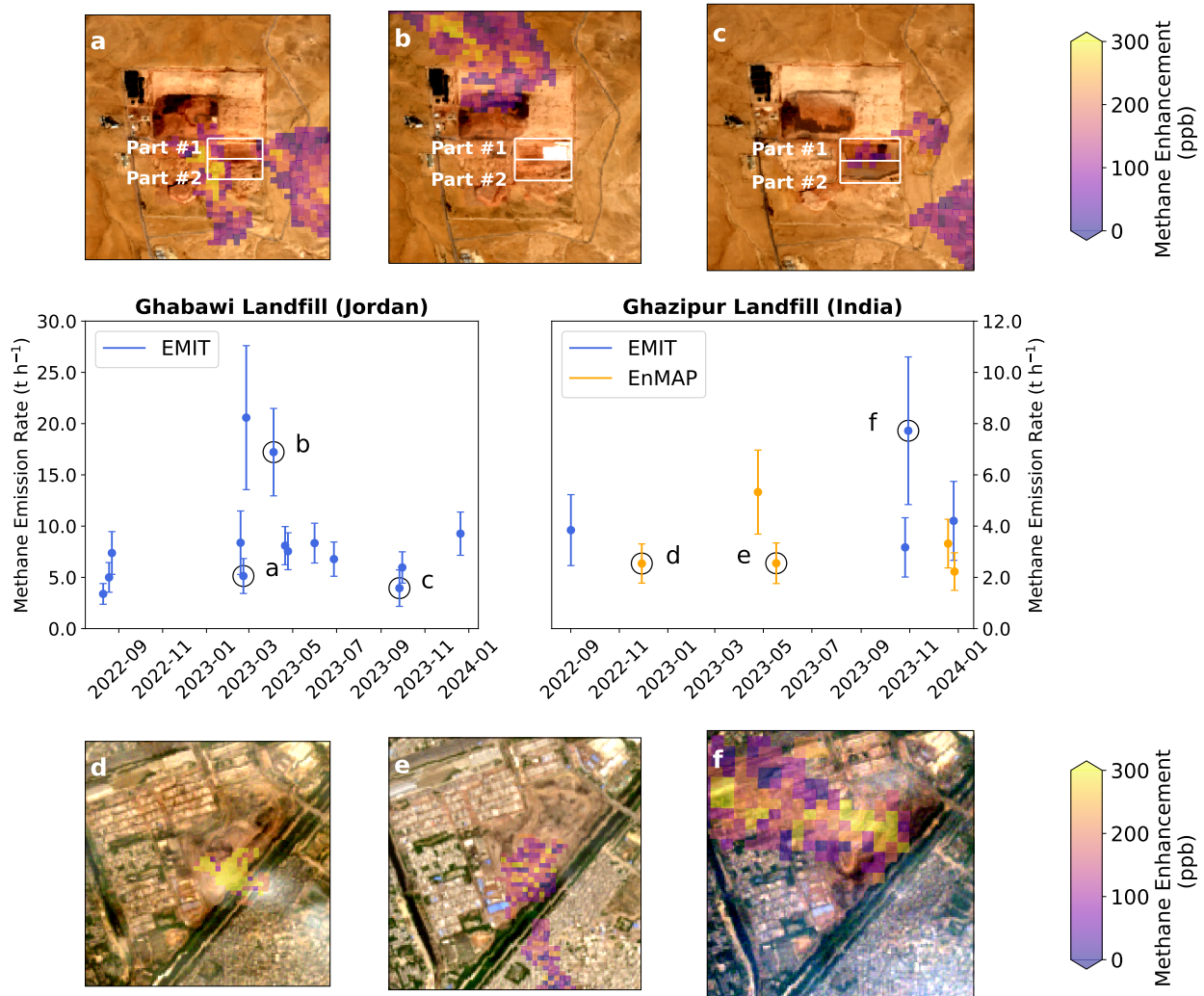


Figure 4: Time series of methane emissions from the Ghabawi (Jordan) and Ghazipur (India) landfills as derived using EMIT and EnMAP data. The complete Sentinel-2 RGB time series for 2023 are available as Movies S1 and S2. The points marked with letters a–f correspond to the insets labeled with matching letters in their upper left corners. (a–c) Methane plumes observed at the Ghabawi landfill shown over Sentinel-2 images³⁸ captured within 3 days of the EMIT overpass: (a) 21 February 2023, (b) 4 April 2023, (c) 26 September 2023. The white rectangles highlight two sections in the newly constructed southern section. (d–f) Similar observations for the Ghazipur landfill: (d) 29 November 2022, (e) 17 May 2023, (f) 30 October 2023.

The variation in emission rates is not correlated with the wind speed magnitude. It is also

seen when using an alternate wind product and quantification method to calculate emission rates (Supplementary Section S1, Figure S15 and S16). We then track waste disposal activities using Sentinel-2 RGB images captured within 3 days of each EMIT overpass (Figure 4 a–c). These images show a shift in the plume source location from the northern cell to a newly established southern cell. The year-round Sentinel-2 images (Figure S17 and Movie S1) show the construction process of the southern cell was divided into two phases: March to June (part #1, Figure 4b) and June to September (part #2, Figure 4c), while waste deposition in the cell began in August. Although the spike in methane emission rates coincides with the active construction of part #1 in April, the plume’s source is not located within this newly constructed area. Instead, it originates from waste deposited in earlier phases of the landfill (Figure 4b). These observations align with previous studies highlighting how variability in landfill emissions is heavily influenced by operational procedures, such as the choice of cover material or alterations in landfill infrastructure, alongside local weather conditions.^{12,39} Retrieval artifacts can also cause minor variations due to the confounding influence of the landfill’s surface materials in the methane retrieval spectral window (2100–2450 nm).

Given the sparse temporal sampling of landfills by individual HSI instruments, combining observations from all available HSI sensors is valuable for exploring emission time series. The Ghazipur landfill in Delhi, India, is an illustrative example (Figure 4 d–f). Despite infrequent revisits, we find that the emission source shifted from the southern section to the northeast, corresponding to increasing activity in the northeastern section, as shown by the Sentinel-2 images (Figure S18 and Movie S2). The combined analysis of HSI data and satellite imagery demonstrates the capability to capture both spatial and temporal changes in landfill operations and associated methane emissions. When more HSI observations become available in the future, they will help us estimate baseline methane emissions more accurately and improve long-term projections of landfill methane emissions.

Discussion

We have analyzed global methane emissions from landfills by integrating observations from TROPOMI and HSIs. TROPOMI first identifies urban hot spots indicative of potentially large landfill methane emissions, which are then targeted by analysis of HSIs. Our findings reveal differences with current landfill emission inventories, highlighting the critical need for observation-based updates to account for super-emitting sites. Furthermore, measurements from different HSIs can be used to monitor emissions over time at any specific site and enable exploring emission variability resulting from operational procedures. This synergistic use of spaceborne sensors establishes a robust framework for continuous global monitoring of landfill methane emissions. Given that 80% of landfill methane emissions could be mitigated through existing technological solutions,^{40,41} our publicly available spaceborne methane emission products can assist efforts to monitor, regulate, and evaluate landfill mitigation strategies.⁵

This study is limited to only the largest emitting hotspots due to TROPOMI's $\sim 8 \text{ t h}^{-1}$ detection threshold.¹⁹ The cumulative distribution of Climate TRACE emissions shows that 5% of global landfill methane emissions can be detected under this constraint (Figure S11b). While this study targets only 0.4% of landfills in the Climate TRACE dataset, these sites account for $\sim 5\%$ of their estimated global landfill emissions (36.8 Tg yr^{-1}), a global total similar to the one from another independent inventory study (31.9 Tg yr^{-1} ;⁴⁰). On the other hand, HSIs detect plumes only from the Tehran landfill among the Climate TRACE landfills emitting more than 8 t h^{-1} , suggesting large facility-level differences.

While the empirical detection limits are 810 kg h^{-1} for EnMAP and 970 kg h^{-1} for EMIT (Supplementary Section S5), this study's lowest two observed emission rates are 900 and $1,050 \text{ kg h}^{-1}$, respectively. Considering the uncertainty of diffuse landfill emissions, we assume a detection threshold of 1 t h^{-1} for HSIs, up to 60% of solid waste emissions could be observable with global monitoring (Figure S11b). Thus, expanding HSI monitoring to more sites by increasing landfill target coverage and implementing automated plume detection^{42,43}

will enable more comprehensive top-down information. Moreover, additional facility-level data will soon become available from satellites designed to observe methane and carbon dioxide, including MethaneSAT ($100 \times 400 \text{ m}^2$ resolution)⁴⁴ and Carbon Mapper ($\sim 35 \text{ m}$ resolution).⁴⁵ To support all these, further validation with controlled releases from landfill-like sources is needed, particularly over complex terrain. As the suite of methane-observing satellites grows, we can improve our understanding of landfill emission distributions and variability, while supporting efforts to mitigate these emissions.

Methods

Hyperspectral Imagers

We combined three push-broom hyperspectral imagers (400–2500 nm) to detect global landfill methane emissions: EMIT,^{33,34} launched on 14 July 2022 and operating on the International Space Station (ISS); EnMAP,^{46,47} launched on 1 April 2022; and PRISMA,^{29,30} launched on 22 March 2019. EnMAP and PRISMA provide 30 m spatial resolution over $30 \times 30 \text{ km}^2$ scenes, while EMIT operates at 60 m resolution but covers a wider 80 km scene. EnMAP and PRISMA are in Sun-Synchronous Low Earth Orbits with equator crossing times of 11:00 and 10:30, respectively, while EMIT has a variable overpass time. At the strong methane absorption window ($\sim 2300 \text{ nm}$), EMIT outperforms EnMAP and PRISMA with a SNR of ~ 500 and a spectral resolution of 7.4 nm.⁴⁸ In contrast, EnMAP’s SNR is twice that of PRISMA (~ 180), and its spectral resolution is 2.7 nm finer than PRISMA’s 10 nm resolution.^{27,49}

Given the substantial size of the hyperspectral datasets, we initially focus on urban hot spots detected by TROPOMI (<https://methanedata.unep.org/>) where the wind rotation technique is used to determine the source location within a few km.^{14,19} Then, we restrict our investigation to the surrounding area to determine whether the detected emissions originate from waste disposal sites or other sources and estimate their emission rates. Additionally, we

analyze observations of the top 20 most emitting landfills from the Climate TRACE dataset.

Methane Enhancement Retrieval

We employ a linearized matched filter technique to retrieve methane enhancements (ΔXCH_4) in parts-per-billion (ppb) from the satellite observations. This approach has been successfully applied before to satellite and aircraft observations.^{26,50–54} The matched filter assumes a spectrally flat background and models the background radiance spectrum as a Gaussian distribution (\mathcal{N}) with a mean vector $\boldsymbol{\mu}$ and a covariance matrix $\boldsymbol{\Sigma}$. The radiance spectrum (L) can be represented by two hypotheses: H_0 for radiance without a methane plume, and H_1 with a plume present.⁵⁰

$$H_0 : L \sim \mathcal{N}(\boldsymbol{\mu}, \boldsymbol{\Sigma}); H_1 : L \sim \mathcal{N}(\boldsymbol{\mu} + \Delta\text{XCH}_4\mathbf{t}, \boldsymbol{\Sigma}) \quad (1)$$

Here, \mathbf{t} represents the target signature, the product of the background mean radiance ($\boldsymbol{\mu}$) and the negative methane absorption coefficient (\mathbf{k}). To determine \mathbf{k} , we employ a forward model⁵⁵ and convolve the radiance with the imager’s central wavelength and FWHM.⁵⁰ The atmosphere is divided into vertical layers with a thickness of 1 km up to an altitude of 25 km, 2.5 km between 25 and 50 km, and 5 km above 50 km altitude. For the forward model simulation, methane enhancements are introduced into the lowest layer at various values, ranging from 0 to 6400 ppb in double increments of 100. The k value (ppb⁻¹) for each band is calculated as the regression slope between the natural logarithm of the radiance and the methane enhancements. The maximum likelihood estimate of the scale factor ΔXCH_4 is:

$$\Delta\text{XCH}_4 = \frac{(\mathbf{t} - \boldsymbol{\mu})^T \boldsymbol{\Sigma}^{-1} (\mathbf{L} - \boldsymbol{\mu})}{(\mathbf{t} - \boldsymbol{\mu})^T \boldsymbol{\Sigma}^{-1} (\mathbf{t} - \boldsymbol{\mu})} \quad (2)$$

The strong absorption window (2100~2450 nm) is selected for the ΔXCH_4 calculation.

However, the results are often noisy in urban areas (due to complicated reflectance related to for example roads and roofs), making it challenging to differentiate plumes from the background. To mitigate this, we perform the same retrieval over the 1300~2500 nm window,⁵⁴ including both the strong (~2300 nm) and weak (~1700 nm) methane absorption windows. Then, we apply a Chambolle total variance denoising (TV) filter⁵⁶ to obtain a smoothed ΔXCH_4 field. The TV filter aims to minimize the cost function between the original and smoothed images. We generate 300 plume-free noisy ΔXCH_4 images and determine the inflection point of the threshold versus denoising weight to exclude all falsely detected plumes.⁵⁷ Considering the lower SNR of PRISMA, we select a denoising weight of 150, higher than the weight of 50 used for EMIT and EnMAP. The two-step denoised ΔXCH_4 field is only used for generating plume masks (Supplementary Section S3), while the emission rate calculation employs the ΔXCH_4 data without denoising.

Emission Rate Quantification

Supplementary Section S3 describes the process for generating a plume mask using the watershedding technique (Figure S4).^{58,59} To account for the possibility of strong and long plumes breaking the sparsity assumption of the matched filter, we exclude the plume pixels in each column of observations. Subsequently, we rerun the retrieval process to obtain the final emission rate products. This two-step approach helps mitigate the impact of dense plumes on the background radiance estimation and typically yields higher methane emission rates.

We then apply the IME method assuming concentrated sources^{60,61} to quantify the methane emission rates (Q in $kg\ h^{-1}$):

$$Q = \frac{U_{\text{eff}} \cdot \text{IME}}{L} \quad (3)$$

where IME is the total methane mass (kg) in the plume mask, L (m) is the square root of the plume area, and U_{eff} is the effective wind speed (m/s). We perform instrument-specific calibrations for U_{eff} based on large-eddy simulations that model emissions from the landfill as an area source (Supplementary Section S3), U_{eff} depends linearly on the 10-m wind speed (U_{10}):

$$\text{EMIT} : U_{\text{eff}} = 0.45 \cdot U_{10} + 0.67 \quad (4)$$

$$\text{EnMAP} : U_{\text{eff}} = 0.37 \cdot U_{10} + 0.69 \quad (5)$$

$$\text{PRISMA} : U_{\text{eff}} = 0.37 \cdot U_{10} + 0.70 \quad (6)$$

Our primary choice for the wind is the European Centre for Medium-Range Weather Forecasts Reanalysis 5 (ERA5) 10-m wind speed. However, we use the GEOS Forward Processing (GEOS-FP) data in cases where the ERA5 wind direction differs from the plume direction by more than 90 degrees. If both the ERA5 and GEOS-FP wind data fail to accurately capture the wind direction, we default to using the ERA5 wind data.

Climate TRACE Bottom-Up Inventory

Climate TRACE is a global greenhouse gas emissions database.⁶² The waste sector component uses Bayesian regression modeling that integrates detailed facility-level waste data from sources such as the US Environmental Protection Agency (EPA),⁶³ Waste Atlas (<http://www.atlas.d-waste.com/>), and Global Plastic Watch (GPW; <https://www.globalplasticwatch.org/>), to estimate methane emissions from solid waste disposal sites globally. The EPA data comes from 2021, while the Waste Atlas data corresponds to 2013, and the GPW data is from 2021. Country-level emissions are generally based on EDGAR estimates, except when the sum of facility-level emissions surpasses the EDGAR-reported figure.

WasteMAP Platform

WasteMAP (<https://wastemap.earth/>) is an online platform that compiles waste methane emission reports, model results, and observations. We only use the city-level data estimated with the bottom-up Solid Waste Emissions Estimation Tool (SWEET) developed by the EPA. SWEET employs environmental factors and waste information from the World Bank What a Waste 2.0 report³ to estimate methane emissions.

Data Availability

The Level 1B data products for EMIT (version 1), EnMAP (version 1.4), and PRISMA (version 1) are available at the following links: <https://search.earthdata.nasa.gov/search?q=C2408009906-LPCLLOUD>, https://www.enmap.org/data_access/, and <https://prisma.asi.it/>. Retrieval and emission data will be available on Zenodo (<https://doi.org/10.5281/zenodo.13643544>). Notebooks to reproduce this work will be deposited on GitHub. HyperGas, the retrieval package, will become open-access following its publication.

Acknowledgement

We thank the Jet Propulsion Laboratory (JPL), German Aerospace Center (DLR), and Italian Space Agency (ASI) for processing the Level 0 data and calibrating the Level 1B radiance data. This work was funded by the Targeting Waste emissions Observed from Space (TWOS) project funded by the Global Methane Hub. S.S. acknowledges funding from the IMEO Science Studies programme contract DTIE22-EN5036. P.T. acknowledges funding from the NSO TROPOMI national program.

Supporting Information Available

- Emission Uncertainty Quantification

- Comparison with Controlled Releases
- IME Calibration and Plume Mask
- Comparison with Carbon Mapper EMIT Quantifications
- Detection Limit

References

- (1) Intergovernmental Panel on Climate Change (IPCC) *Climate Change 2021 – The Physical Science Basis: Working Group I Contribution to the Sixth Assessment Report of the Intergovernmental Panel on Climate Change*; Cambridge University Press: Cambridge, 2023.
- (2) Saunio, M. et al. The Global Methane Budget 2000–2017. *Earth Syst. Sci. Data* **2020**, *12*, 1561–1623.
- (3) Kaza, S.; Yao, L. C.; Bhada-Tata, P.; Van Woerden, F. *What a Waste 2.0*; Washington, DC: World Bank, 2018.
- (4) COP29 Declaration on Reducing Methane from Organic Waste. <https://cop29.az/en/pages/cop29-declaration-on-reducing-methane-from-organic-waste>.
- (5) Bureau of Oceans and International Environmental and Scientific Affairs Lowering Organic Waste Methane Initiative (LOW-Methane). <https://www.state.gov/lowering-organic-waste-methane-initiative-low-methane/>, 2023.
- (6) Duren, R. M. et al. California’s Methane Super-Emitters. *Nature* **2019**, *575*, 180–184.
- (7) Solazzo, E.; Crippa, M.; Guizzardi, D.; Muntean, M.; Choulga, M.; Janssens-Maenhout, G. Uncertainties in the Emissions Database for Global Atmospheric Re-

- search (EDGAR) Emission Inventory of Greenhouse Gases. *Atmos. Chem. Phys.* **2021**, *21*, 5655–5683.
- (8) Cusworth, D. H. et al. Quantifying Methane Emissions from United States Landfills. *Sci. Adv.* **2024**, *383*, 1499–1504.
- (9) Wang, Y.; Fang, M.; Lou, Z.; He, H.; Guo, Y.; Pi, X.; Wang, Y.; Yin, K.; Fei, X. Methane Emissions from Landfills Differentially Underestimated Worldwide. *Nat. Sustain* **2024**, *7*, 496–507.
- (10) Miller, S. M.; Wofsy, S. C.; Michalak, A. M.; Kort, E. A.; Andrews, A. E.; Biraud, S. C.; Dlugokencky, E. J.; Eluszkiewicz, J.; Fischer, M. L.; Janssens-Maenhout, G.; Miller, B. R.; Miller, J. B.; Montzka, S. A.; Nehrkorn, T.; Sweeney, C. Anthropogenic Emissions of Methane in the United States. *Proc. Natl. Acad. Sci.* **2013**, *110*, 20018–20022.
- (11) Singh, C. K.; Kumar, A.; Roy, S. S. Quantitative Analysis of the Methane Gas Emissions from Municipal Solid Waste in India. *Sci. Rep.* **2018**, *8*, 2913.
- (12) Cusworth, D. H.; Duren, R. M.; Thorpe, A. K.; Tseng, E.; Thompson, D.; Guha, A.; Newman, S.; Foster, K. T.; Miller, C. E. Using Remote Sensing to Detect, Validate, and Quantify Methane Emissions from California Solid Waste Operations. *Environ. Res. Lett.* **2020**, *15*, 054012.
- (13) Spokas, K.; Bogner, J.; Corcoran, M. Modeling Landfill CH₄ Emissions: CALMIM International Field Validation, Using CALMIM to Simulate Management Strategies, Current and Future Climate Scenarios. *Elem. Sci. Anth.* **2021**, *9*, 00050.
- (14) Maasackers, J. D.; Varon, D. J.; Elfarsdóttir, A.; McKeever, J.; Jarvis, D.; Mahapatra, G.; Pandey, S.; Lorente, A.; Borsdorff, T.; Foorthuis, L. R.; Schuit, B. J.; Tol, P.; van Kempen, T. A.; van Hees, R.; Aben, I. Using Satellites to Uncover Large Methane Emissions from Landfills. *Sci. Adv.* **2022**, *8*, eabn9683.

- (15) Veefkind, J. P. et al. TROPOMI on the ESA Sentinel-5 Precursor: A GMES Mission for Global Observations of the Atmospheric Composition for Climate, Air Quality and Ozone Layer Applications. *Remote Sens. Environ.* **2012**, *120*, 70–83.
- (16) Lorente, A. et al. Methane Retrieved from TROPOMI: Improvement of the Data Product and Validation of the First 2 Years of Measurements. *Atmos. Meas. Tech.* **2021**, *14*, 665–684.
- (17) Zhang, Y. et al. Quantifying Methane Emissions from the Largest Oil-Producing Basin in the United States from Space. *Sci. Adv.* **2020**, *6*, eaaz5120.
- (18) Shen, L.; Jacob, D. J.; Gautam, R.; Omara, M.; Scarpelli, T. R.; Lorente, A.; Zavala-Araiza, D.; Lu, X.; Chen, Z.; Lin, J. National Quantifications of Methane Emissions from Fuel Exploitation Using High Resolution Inversions of Satellite Observations. *Nat. Commun.* **2023**, *14*, 4948.
- (19) Schuit, B. J. et al. Automated Detection and Monitoring of Methane Super-Emitters Using Satellite Data. *Atmos. Chem. Phys.* **2023**, *23*, 9071–9098.
- (20) Varon, D. J.; McKeever, J.; Jervis, D.; Maasackers, J. D.; Pandey, S.; Houweling, S.; Aben, I.; Scarpelli, T.; Jacob, D. J. Satellite Discovery of Anomalously Large Methane Point Sources From Oil/Gas Production. *Geophys. Res. Lett.* **2019**, *46*, 13507–13516.
- (21) Dogniaux, M.; Maasackers, J. D.; Girard, M.; Jervis, D.; McKeever, J.; Schuit, B. J.; Sharma, S.; Lopez-Noreña, A.; Varon, D. J.; Aben, I. Satellite Survey Sheds New Light on Global Solid Waste Methane Emissions. *Preprint at <https://doi.org/10.31223/X5TB09>* **2024**,
- (22) Varon, D. J.; Jervis, D.; McKeever, J.; Spence, I.; Gains, D.; Jacob, D. J. High-Frequency Monitoring of Anomalous Methane Point Sources with Multispectral Sentinel-2 Satellite Observations. *Atmos. Meas. Tech.* **2021**, *14*, 2771–2785.

- (23) Pandey, S.; van Nistelrooij, M.; Maasackers, J. D.; Sutar, P.; Houweling, S.; Varon, D. J.; Tol, P.; Gains, D.; Worden, J.; Aben, I. Daily Detection and Quantification of Methane Leaks Using Sentinel-3: A Tiered Satellite Observation Approach with Sentinel-2 and Sentinel-5p. *Remote Sens. Environ.* **2023**, *296*, 113716.
- (24) Watine-Guiu, M.; Varon, D. J.; Irakulis-Loitxate, I.; Balasus, N.; Jacob, D. J. Geostationary Satellite Observations of Extreme and Transient Methane Emissions from Oil and Gas Infrastructure. *Proc. Natl. Acad. Sci.* **2023**, *120*, e2310797120.
- (25) Guanter, L.; Irakulis-Loitxate, I.; Gorroño, J.; Sánchez-García, E.; Cusworth, D. H.; Varon, D. J.; Cogliati, S.; Colombo, R. Mapping Methane Point Emissions with the PRISMA Spaceborne Imaging Spectrometer. *Remote Sens. Environ.* **2021**, *265*, 112671.
- (26) Thorpe, A. K. et al. Attribution of Individual Methane and Carbon Dioxide Emission Sources Using EMIT Observations from Space. *Sci. Adv.* **2023**, *9*, eadh2391.
- (27) Roger, J.; Irakulis-Loitxate, I.; Valverde, A.; Gorroño, J.; Chabrilat, S.; Brell, M.; Guanter, L. High-Resolution Methane Mapping with the EnMAP Satellite Imaging Spectroscopy Mission. *IEEE Trans. Geosci. Remote Sens.* **2024**, *62*, 1–12.
- (28) Thorpe, A. K.; O’Handley, C.; Emmitt, G. D.; DeCola, P. L.; Hopkins, F. M.; Yadav, V.; Guha, A.; Newman, S.; Herner, J. D.; Falk, M.; Duren, R. M. Improved Methane Emission Estimates Using AVIRIS-NG and an Airborne Doppler Wind Lidar. *Remote Sens. Environ.* **2021**, *266*, 112681.
- (29) Loizzo, R.; Guarini, R.; Longo, F.; Scopa, T.; Formaro, R.; Facchinetti, C.; Varacalli, G. Prisma: The Italian Hyperspectral Mission. 2018.
- (30) Cogliati, S. et al. The PRISMA Imaging Spectroscopy Mission: Overview and First Performance Analysis. *Remote Sens. Environ.* **2021**, *262*, 112499.

- (31) Sherwin, E. D.; Rutherford, J. S.; Chen, Y.; Aminfard, S.; Kort, E. A.; Jackson, R. B.; Brandt, A. R. Single-Blind Validation of Space-Based Point-Source Detection and Quantification of Onshore Methane Emissions. *Sci. Rep.* **2023**, *13*, 3836.
- (32) Sherwin, E. D.; El Abbadi, S. H.; Burdeau, P. M.; Zhang, Z.; Chen, Z.; Rutherford, J. S.; Chen, Y.; Brandt, A. R. Single-Blind Test of Nine Methane-Sensing Satellite Systems from Three Continents. *Atmos. Meas. Tech.* **2024**, *17*, 765–782.
- (33) Green, R. O. et al. The Earth Surface Mineral Dust Source Investigation: An Earth Science Imaging Spectroscopy Mission. 2020.
- (34) Green, R. O. et al. Performance and Early Results from the Earth Surface Mineral Dust Source Investigation (EMIT) Imaging Spectroscopy Mission. 2023.
- (35) Esri; Maxar; Geographics, E.; the GIS User Community ESRI World Imagery. https://services.arcgisonline.com/ArcGIS/rest/services/World_Imagery/MapServer, 2022.
- (36) Toha, M.; Rahman, M. M. Estimation and Prediction of Methane Gas Generation from Landfill Sites in Dhaka City, Bangladesh. *Case Stud. Chem. Environ. Eng.* **2023**, *7*, 100302.
- (37) Carbon Mapper data Retrieved from <https://data.carbonmapper.org>. 2024.
- (38) Sentinel-2 Cloud-Optimized GeoTIFFs. <https://registry.opendata.aws/sentinel-2-l2a-cogs/>, 2024.
- (39) Karion, A.; Ghosh, S.; Lopez-Coto, I.; Mueller, K.; Gourdji, S.; Pitt, J.; Whetstone, J. Methane Emissions Show Recent Decline but Strong Seasonality in Two US Northeastern Cities. *Environ. Sci. Technol.* **2023**, *57*, 19565–19574.
- (40) Höglund-Isaksson, L.; Gómez-Sanabria, A.; Klimont, Z.; Rafaj, P.; Schöpp, W. Technical Potentials and Costs for Reducing Global Anthropogenic Methane Emissions in

- the 2050 Timeframe –Results from the GAINS Model. *Environ. Res. Commun.* **2020**, *2*, 025004.
- (41) Ocko, I. B.; Sun, T.; Shindell, D.; Oppenheimer, M.; Hristov, A. N.; Pacala, S. W.; Mauzerall, D. L.; Xu, Y.; Hamburg, S. P. Acting Rapidly to Deploy Readily Available Methane Mitigation Measures by Sector Can Immediately Slow Global Warming. *Environ. Res. Lett.* **2021**, *16*, 054042.
- (42) Růžička, V.; Mateo-Garcia, G.; Gómez-Chova, L.; Vaughan, A.; Guanter, L.; Markham, A. Semantic Segmentation of Methane Plumes with Hyperspectral Machine Learning Models. *Sci. Rep.* **2023**, *13*, 19999.
- (43) Kumar, S.; Arevalo, I.; Iftekhar, ASM.; Manjunath, BS. Methanemapper: Spectral Absorption Aware Hyperspectral Transformer for Methane Detection. 2023.
- (44) Rohrschneider, R.; Wofsy, S.; Franklin, J.; Benmergui, J.; Soto, J.; Davis, S. The MethaneSAT Mission. *Small Satellite Conference* **2021**,
- (45) Keremedjiev, M.; Haag, J.; Shivers, S.; Guido, J.; Roth, K.; teja Nallapu, R.; Dockstader, S.; McGill, L.; Giuliano, P.; Duren, R.; Asner, G. P. Carbon Mapper Phase 1: Two Upcoming VNIR-SWIR Hyperspectral Imaging Satellites. 2022.
- (46) Guanter, L. et al. The EnMAP Spaceborne Imaging Spectroscopy Mission for Earth Observation. *Remote Sens.* **2015**, *7*, 8830–8857.
- (47) Storch, T. et al. The EnMAP Imaging Spectroscopy Mission towards Operations. *Remote Sens. Environ.* **2023**, *294*, 113632.
- (48) Thompson, D. R. et al. On-Orbit Calibration and Performance of the EMIT Imaging Spectrometer. *Remote Sens. Environ.* **2024**, *303*, 113986.
- (49) Cusworth, D. H.; Jacob, D. J.; Varon, D. J.; Chan Miller, C.; Liu, X.; Chance, K.; Thorpe, A. K.; Duren, R. M.; Miller, C. E.; Thompson, D. R.; Frankenberg, C.; Guan-

- ter, L.; Randles, C. A. Potential of Next-Generation Imaging Spectrometers to Detect and Quantify Methane Point Sources from Space. *Atmos. Meas. Tech.* **2019**, *12*, 5655–5668.
- (50) Thompson, D. R.; Leifer, I.; Bovensmann, H.; Eastwood, M.; Fladeland, M.; Frankenberg, C.; Gerilowski, K.; Green, R. O.; Kratwurst, S.; Krings, T.; Luna, B.; Thorpe, A. K. Real-Time Remote Detection and Measurement for Airborne Imaging Spectroscopy: A Case Study with Methane. *Atmos. Meas. Tech.* **2015**, *8*, 4383–4397.
- (51) Thompson, D. R.; Thorpe, A. K.; Frankenberg, C.; Green, R. O.; Duren, R.; Gunter, L.; Hollstein, A.; Middleton, E.; Ong, L.; Ungar, S. Space-Based Remote Imaging Spectroscopy of the Aliso Canyon CH₄ Superemitter. *Geophys. Res. Lett.* **2016**, *43*, 6571–6578.
- (52) Foote, M. D.; Dennison, P. E.; Thorpe, A. K.; Thompson, D. R.; Jongaramrungruang, S.; Frankenberg, C.; Joshi, S. C. Fast and Accurate Retrieval of Methane Concentration From Imaging Spectrometer Data Using Sparsity Prior. *IEEE Trans. Geosci. Remote Sens.* **2020**, *58*, 6480–6492.
- (53) Foote, M. D.; Dennison, P. E.; Sullivan, P. R.; O’Neill, K. B.; Thorpe, A. K.; Thompson, D. R.; Cusworth, D. H.; Duren, R.; Joshi, S. C. Impact of Scene-Specific Enhancement Spectra on Matched Filter Greenhouse Gas Retrievals from Imaging Spectroscopy. *Remote Sens. Environ.* **2021**, *264*, 112574.
- (54) Roger, J.; Gunter, L.; Gorroño, J.; Irakulis-Loitxate, I. Exploiting the Entire Near-Infrared Spectral Range to Improve the Detection of Methane Plumes with High-Resolution Imaging Spectrometers. *Atmos. Meas. Tech.* **2024**, *17*, 1333–1346.
- (55) Gloudemans, A. M. S.; Schrijver, H.; Hasekamp, O. P.; Aben, I. Error Analysis for CO and CH₄ Total Column Retrievals from SCIAMACHY 2.3 μm Spectra. *Atmos. Chem. Phys.* **2008**, *8*, 3999–4017.

- (56) Chambolle, A. An Algorithm for Total Variation Minimization and Applications. *J. Math. Imaging Vis.* **2004**, *20*, 89–97.
- (57) Chan Miller, C. et al. Methane Retrieval from MethaneAIR Using the CO₂ Proxy Approach: A Demonstration for the Upcoming MethaneSAT Mission. *Atmos. Meas. Tech.* **2024**, *17*, 5429–5454.
- (58) Heikenfeld, M.; Marinescu, P. J.; Christensen, M.; Watson-Parris, D.; Senf, F.; van den Heever, S. C.; Stier, P. Tobac 1.2: Towards a Flexible Framework for Tracking and Analysis of Clouds in Diverse Datasets. *Geosci. Model Dev.* **2019**, *12*, 4551–4570.
- (59) Zhang, X.; van der A, R.; Ding, J.; Eskes, H.; van Geffen, J.; Yin, Y.; Anema, J.; Vagasky, C.; L. Lapierre, J.; Kuang, X. Spaceborne Observations of Lightning NO₂ in the Arctic. *Environ. Sci. Technol.* **2023**, *57*, 2322–2332.
- (60) Frankenberg, C.; Thorpe, A. K.; Thompson, D. R.; Hulley, G.; Kort, E. A.; Vance, N.; Borchardt, J.; Krings, T.; Gerilowski, K.; Sweeney, C.; Conley, S.; Bue, B. D.; Aubrey, A. D.; Hook, S.; Green, R. O. Airborne Methane Remote Measurements Reveal Heavy-Tail Flux Distribution in Four Corners Region. *Proc. Natl. Acad. Sci.* **2016**, *113*, 9734–9739.
- (61) Varon, D. J.; Jacob, D. J.; McKeever, J.; Jarvis, D.; Durak, B. O. A.; Xia, Y.; Huang, Y. Quantifying Methane Point Sources from Fine-Scale Satellite Observations of Atmospheric Methane Plumes. *Atmos. Meas. Tech.* **2018**, *11*, 5673–5686.
- (62) Climate TRACE - Tracking Real-time Atmospheric Carbon Emissions Climate TRACE Emissions Inventory. 2024.
- (63) US EPA, OAR. Inventory of U.S. Greenhouse Gas Emissions and Sinks: 1990–2021. <https://www.epa.gov/ghgemissions/inventory-us-greenhouse-gas-emissions-and-sinks-1990-2021>, 2023.

Supporting Information for "Global Identification of Solid Waste Methane Super Emitters using Hyperspectral Satellites"

Xin Zhang,^{*,†} Joannes D. Maasakkers,[†] Javier Roger,[‡] Luis Guanter,^{‡,¶} Shubham Sharma,[†] Srijana Lama,[†] Paul Tol,[†] Daniel J. Varon,[§] Daniel H. Cusworth,^{||} Katherine Howell,^{||} Andrew K. Thorpe,[⊥] Philip G. Brodrick,[⊥] and Ilse Aben^{†,#}

[†]*SRON Netherlands Institute for Space Research, Leiden, 2333 CA, The Netherlands*

[‡]*Research Institute of Water and Environmental Engineering, Universitat Politècnica de València, Valencia 46022, Spain*

[¶]*Environmental Defense Fund, Amsterdam, 1083 HN, The Netherlands*

[§]*School of Engineering and Applied Sciences, Harvard University, Cambridge, 02138, MA, USA*

^{||}*Carbon Mapper, Pasadena, 91105, CA, USA*

[⊥]*Jet Propulsion Laboratory, California Institute of Technology, Pasadena, 91109, CA, USA*

[#]*Department of Earth Sciences, Vrije Universiteit Amsterdam, Amsterdam, 1081 HV, The Netherlands*

E-mail: xin.zhang@sron.nl

1	Contents	
2	S1 Emission Uncertainty Quantification	S3
3	S2 Comparison with Controlled Releases	S5
4	S3 IME Calibration and Plume Mask	S5
5	S4 Comparison with Carbon Mapper EMIT Quantifications	S9
6	S5 Detection Limit	S10
7	S6 Supplementary Figures and Tables	S12
8	References	S30
9	Number of figures: 18	
10	Number of tables: 7	

11 S1 Emission Uncertainty Quantification

12 There are three sources of uncertainty in our emission uncertainty estimations: wind speed
13 error, retrieval random error, and uncertainty in the integrated mass enhancement (IME)
14 calibration.¹⁻³ For the error in the wind speed, we compare the European Centre for Medium-
15 Range Weather Forecasts Reanalysis 5 (ERA5) 10-m wind data with the automated Surface
16 Observing System (ASOS) dataset obtained from worldwide airports ([https://mesonet.
18 agron.iastate.edu/ASOS/](https://mesonet.
17 agron.iastate.edu/ASOS/)). We only include the wind data recorded between 10:00 and
19 14:00 (local time) to coincide with HSI overpass times. The standard deviation of the
20 difference between ERA5 and ASOS wind data, is $\sim 1.5 \text{ m s}^{-1}$ for wind speeds higher than
21 3 m/s. For wind speeds lower than 3 m/s, we apply a relative wind error of 50%.⁴ We also
22 compare the ERA5 and GEOS Forward Processing (GEOS-FP) wind reanalysis data and
find that their difference falls within our wind uncertainty estimate.

23 To quantify the effects of retrieval random error, we apply the plume mask to non-plume
24 pixels across the entire scene and calculate the standard deviation of the emission rates.¹
25 The last component of uncertainty is the IME calibration (Section S3) error. The area-
26 source calibration that we use assumes a uniform distribution of methane emissions across
27 a $275 \times 275 \text{ m}^2$ area, whereas the real distribution can be more complex.³ To estimate the
28 uncertainty originating from this simplification, we change the effective wind calibration to
29 one that is calibrated using point sources and calculate the resulting change in emission
30 rate.³

31 Overall, the uncertainties associated with wind speed error, retrieval random error, and
32 IME calibration error are 24%, 15%, and 16%, respectively (Fig. S1). To estimate the un-
33 certainty in individual estimates or summation of methane emissions from different landfills,
34 we calculate the square root of the sum of the squares of the individual uncertainties.

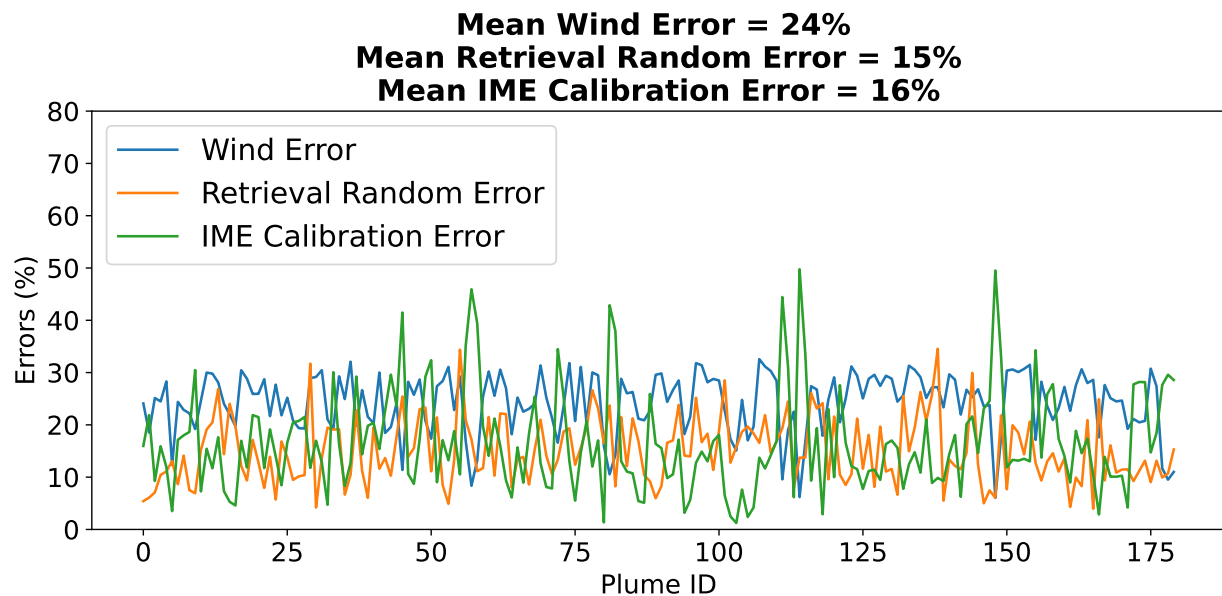


Figure S1: Relative estimation uncertainties from wind (blue), retrieval random error (orange), and IME calibration error (green). The wind error is set as 1.5 m s^{-1} for wind speeds higher than 3 m/s , while it is 50% for wind speeds lower than 3 m/s . The random error is estimated using the standard deviation of emission rates obtained by shifting the plume mask to non-plume pixels across the entire scene. The plume IDs on the x-axis are arranged chronologically.

35 S2 Comparison with Controlled Releases

36 We validate our emission quantification by comparing the derived emission rates with con-
37 trolled methane releases conducted in 2021 and 2022 (Fig. S2). For the EnMAP controlled
38 release, the actual release rate was 1.1 t h^{-1} , while our estimation yields $1.6 \pm 0.5 \text{ t h}^{-1}$,
39 which agrees with the estimations from other analysis teams ranging from 1.5 to 1.8 t h^{-1} .⁵
40 Similarly, for the PRISMA controlled release, our estimation is $5.2 \pm 1.8 \text{ t h}^{-1}$, while the
41 actual release rate was 4.5 t h^{-1} , and other analysis teams estimated emission rates within
42 the range of 3.6 to 5.0 t h^{-1} .⁶

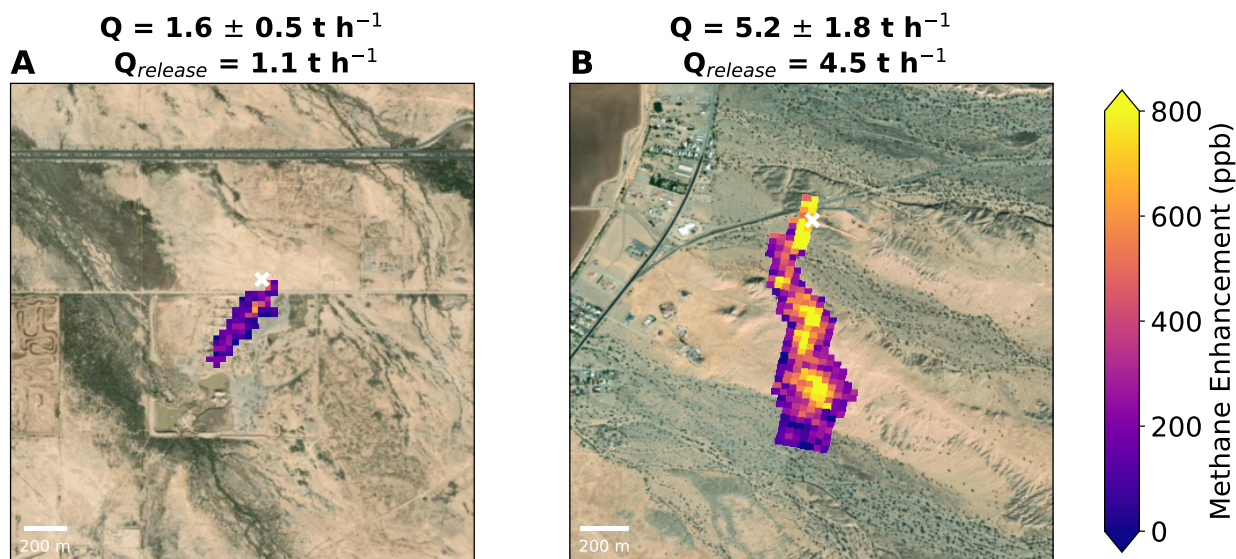


Figure S2: Methane enhancements observed by (A) EnMAP on November 16, 2022, and (B) PRISMA on October 21, 2021, for two controlled methane release experiments.^{5,6} Our estimates $1.6 \pm 0.5 \text{ t h}^{-1}$ and $5.2 \pm 1.8 \text{ t h}^{-1}$ compare well with the actual releases of 1.1 t h^{-1} and 4.5 t h^{-1} respectively. The release sites are marked with a white 'x'. Background imagery comes from Esri World Imagery.⁷

43 S3 IME Calibration and Plume Mask

44 To calibrate the effective wind speed used in the IME calculation against reanalysis 10 m
45 wind speeds, we employ Weather and Research Model large-eddy simulations (WRF-LES)
46 for two source types: a $275 \times 275 \text{ m}^2$ area source (e.g., like a landfill³) and a point source

47 (e.g., oil & gas and underground coal mining facilities). We randomly scale source rates
48 from 1 to 30 t h⁻¹ and add normally distributed measurement noise (Fig. S3A). Noise
49 levels are defined by standard deviations of non-plume methane enhancement in clear-sky
50 hyperspectral scenes, with precisions of 3%, 5%, and 12% for EMIT, EnMAP, and PRISMA,
51 respectively. For each plume, the effective wind speed (U_{eff}) is computed from QL/IME ,
52 where the emission rate (Q) is known, and plume length (L , square root of the plume area)
53 and IME are calculated from plume masks.

54 We derive methane plume masks by applying a watershedding technique to denoised
55 methane fields (Fig. S3B). This method has been applied to track convective clouds⁸ and
56 nitrogen dioxide plumes in TROPOMI observations.⁹ It treats pixel values as a topographic
57 surface and separates them into catchment basins. Threshold values of 2 and 3 standard
58 deviations are used to identify multiple localized high-enhancement features and nearby
59 areas with high enhancement values (Fig. S3C). We dilate these masks by 180 m and merge
60 overlapping masks, with the mask containing the emission source used to identify masks from
61 a single source (Fig. S3D). Figure S4 demonstrates the plume mask determined for a Norte
62 III landfill methane emission plume. To ensure plumes originate from the same source, we
63 limit the azimuth difference of the oriented envelope (minimum rotated rectangle) to less than
64 30° (Fig. S4C), assuming minimal wind direction changes around the landfill. Non-detects
65 are classified if no plume mask covers the source of interest.

66 Figure S5 shows the relationship between U_{eff} and U_{10} inferred from the LES ensemble.
67 We use the area-source calibration by default and the point-source calibration to estimate
68 calibration error.

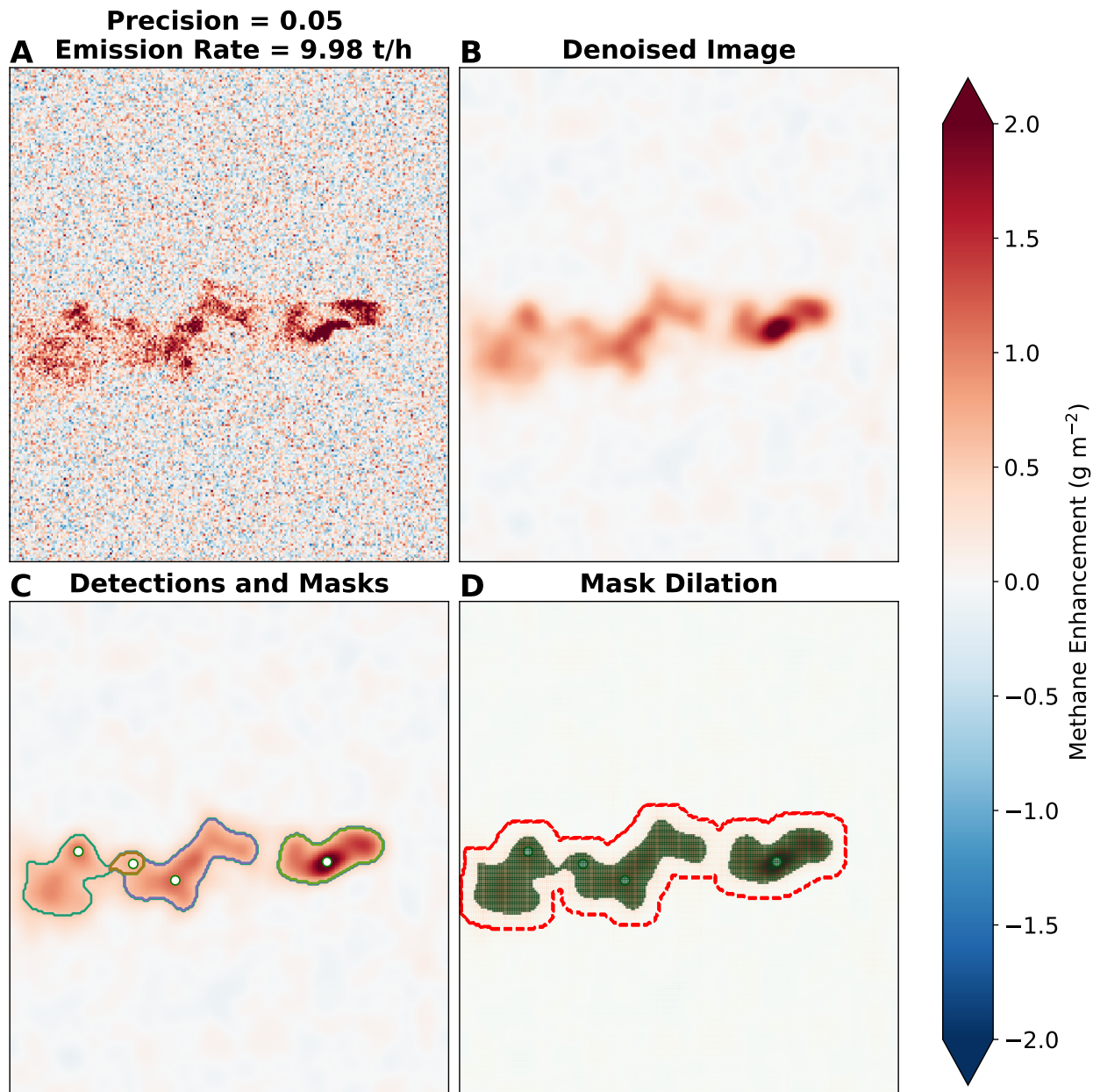


Figure S3: Plume mask generation process for methane emissions using WRF-LES simulation. (A) Methane enhancement (ΔXCH_4) with added Gaussian noise ($\sigma=0.05 \times 1875$ ppb). (B) Denoised ΔXCH_4 field after applying a Chambolle total variation (TV) denoising filter. (C) Initial plume masks derived from the watershedding algorithm. White dots indicate high- ΔXCH_4 locations; contours represent individual masks. (D) Final plume mask (dark green): initial masks expanded by 180 m and combined (red).

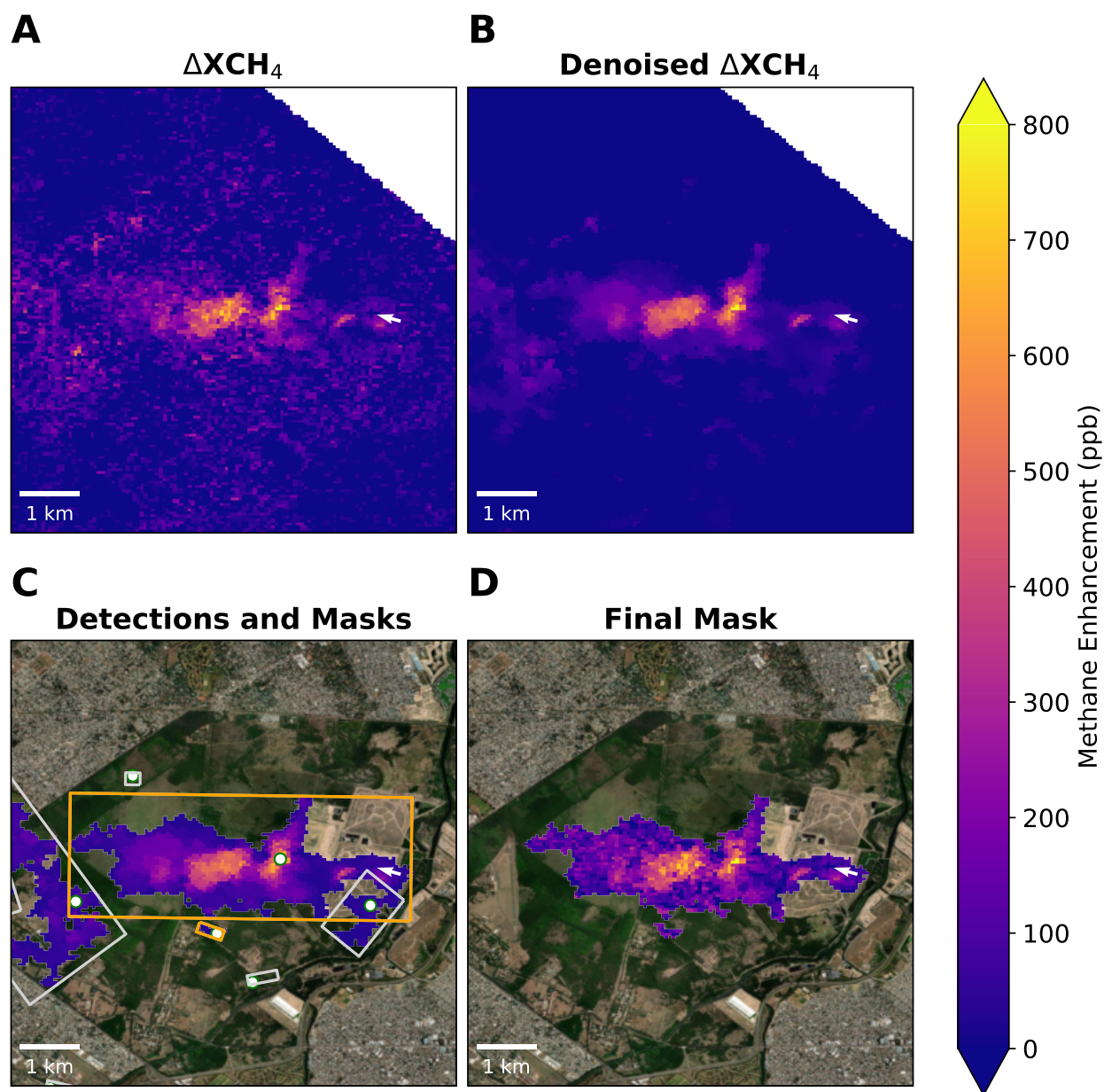


Figure S4: Plume mask creation process for the Norte III landfill methane emission using the EMIT observation on November 24, 2023. The white pixels represent missing data (outside the EMIT image swath), while the white arrow indicates the ERA5 wind direction. (A) Methane enhancement (ΔXCH_4) derived from the strong CH_4 absorption window (2100~2450 nm). (B) Denoised ΔXCH_4 field obtained by applying the Chambolle total variance denoising (TV) filter to ΔXCH_4 within the 1300~2500 nm window. (C) Initial plume masks derived from watershedding algorithm. White dots indicate high- ΔXCH_4 locations; rectangles represent the minimum rotated rectangles for each mask, with orange rectangles indicating azimuth differences less than 30° . (D) Final ΔXCH_4 plume mask.

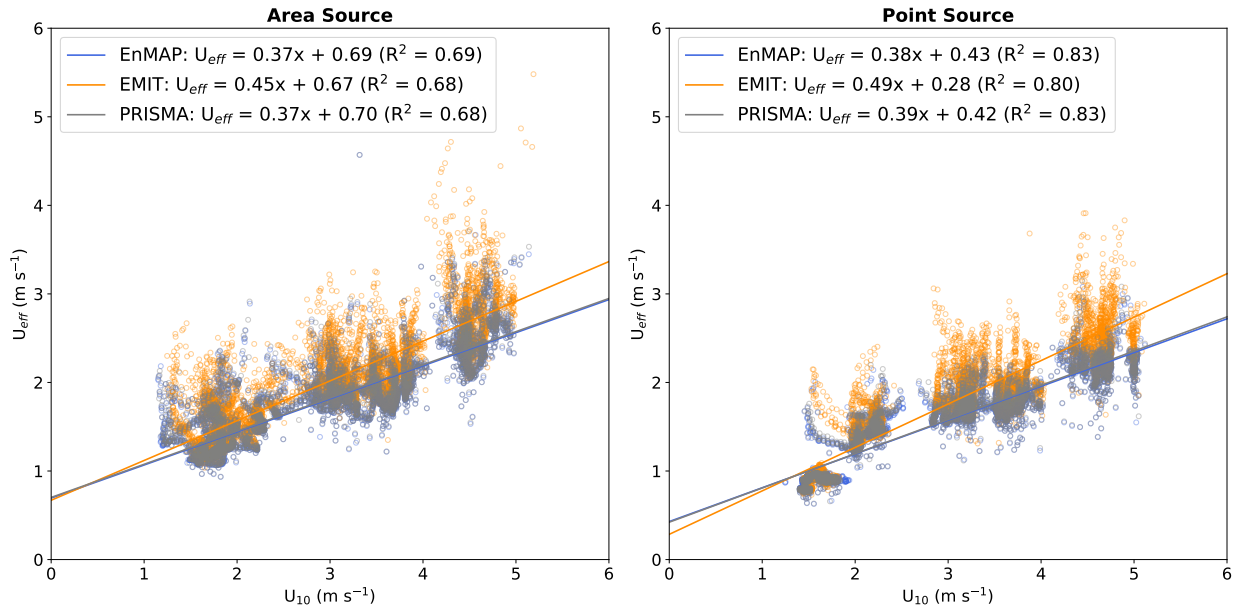


Figure S5: Relationship between the effective and local 10 m wind speeds for different instrument precisions and source types based on WRF LES simulations.

S4 Comparison with Carbon Mapper EMIT Quantifications

Carbon Mapper (<https://data.carbonmapper.org>) provides methane emission rate estimates for EMIT using a method we call 'IME-fetch', which only uses the first 2500 m of the plume to perform the quantification. We apply this method and compare the results to our IME results. The IME-fetch method consists of the following steps: 1) Center the Level 2B methane enhancement map on the plume origin, covering an area of ± 2500 m in both horizontal directions. 2) Use a 90th percentile threshold with a 1000 m crop to distinguish between the background and plume enhancements. Identify pixels exceeding this threshold and group them into connected clusters. Consider only clusters with at least 5 pixels as part of the plume. 3) Apply a proximity criterion to each cluster group, excluding separated clusters more than 15 pixels away from the plume origin. The emission rate is calculated as $\text{IME-fetch} \cdot U_{10} / L$, where U_{10} is the mean 10 m wind speed in the plume mask (the method does not rely on an effective wind speed) and L is the maximum distance from the plume

83 origin to another point along the segmented plume’s convex hull.

84 Figure S6A compares source rates retrieved from both IME and IME-fetch methods
85 to the true source rates from WRF-LES. While the IME method shows good agreement
86 (slope=0.99, $R^2=0.93$) due to calibration, the IME-fetch results underestimate the emission
87 rates (slope=0.77, $R^2=0.89$). This disagreement is mainly due to differences in used plume
88 length (Fig. S6B), which depends on the plume masking method. Our IME method (Section
89 S3) uses a smoother plume mask without fetch distance limitations, leading to more plume
90 pixels for longer plumes. This trend is also observed in real EMIT observations (Fig. S6C),
91 but with greater magnitude. Further research is needed to accurately reproduce both trend
92 and magnitude, which will help address potential biases in quantification.

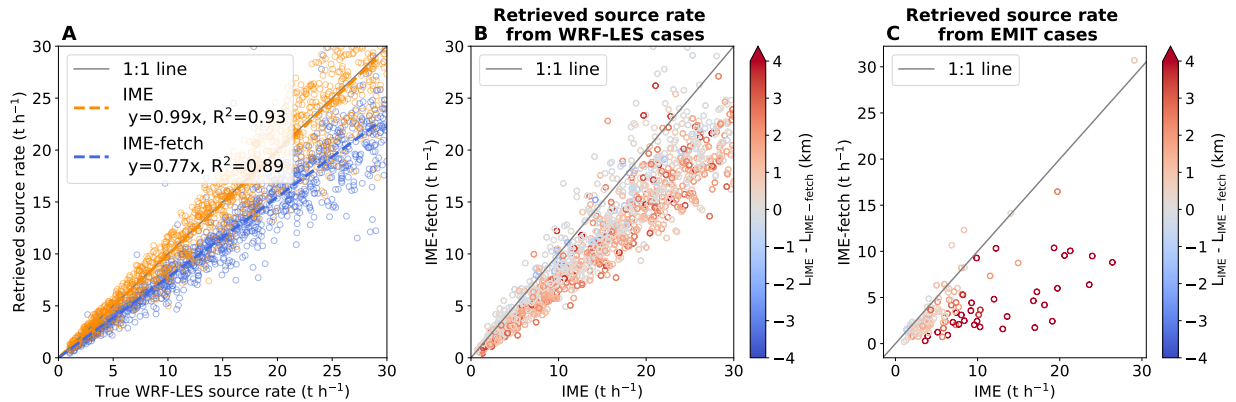


Figure S6: (A) Comparison of the IME (this study) and IME-fetch (Carbon Mapper) methods for estimating source rates using the WRF-LES test set for EMIT. (B) Correlation between IME and IME-fetch values as a function of plume length difference. (C) Same as (B), but from 127 EMIT observations over 36 landfills in this study.

93 S5 Detection Limit

94 The theoretical point-source methane detection limit (Q_{min}) of instruments can be derived
95 from:

$$Q_{min} = PUGq \tag{1}$$

96 where P is the methane precision (kg m^{-2} , see Section S3), U is the mean wind speed (3
97 m s^{-2} used here), G is the ground sampling distance (m), and q is a constant equal to 5 for
98 quantification.^{10,11} This results in detection limits of 810 kg h^{-1} for EnMAP and 970 kg h^{-1}
99 for EMIT. For the EnMAP observations in this study, we find one plume with an emission
100 rate below 1 t h^{-1} and 8 plumes with emission rates between 1 and 2 t h^{-1} . The EMIT data
101 show 10 plumes with emission rates between 1 and 2 t h^{-1} , but none below 1 t h^{-1} .

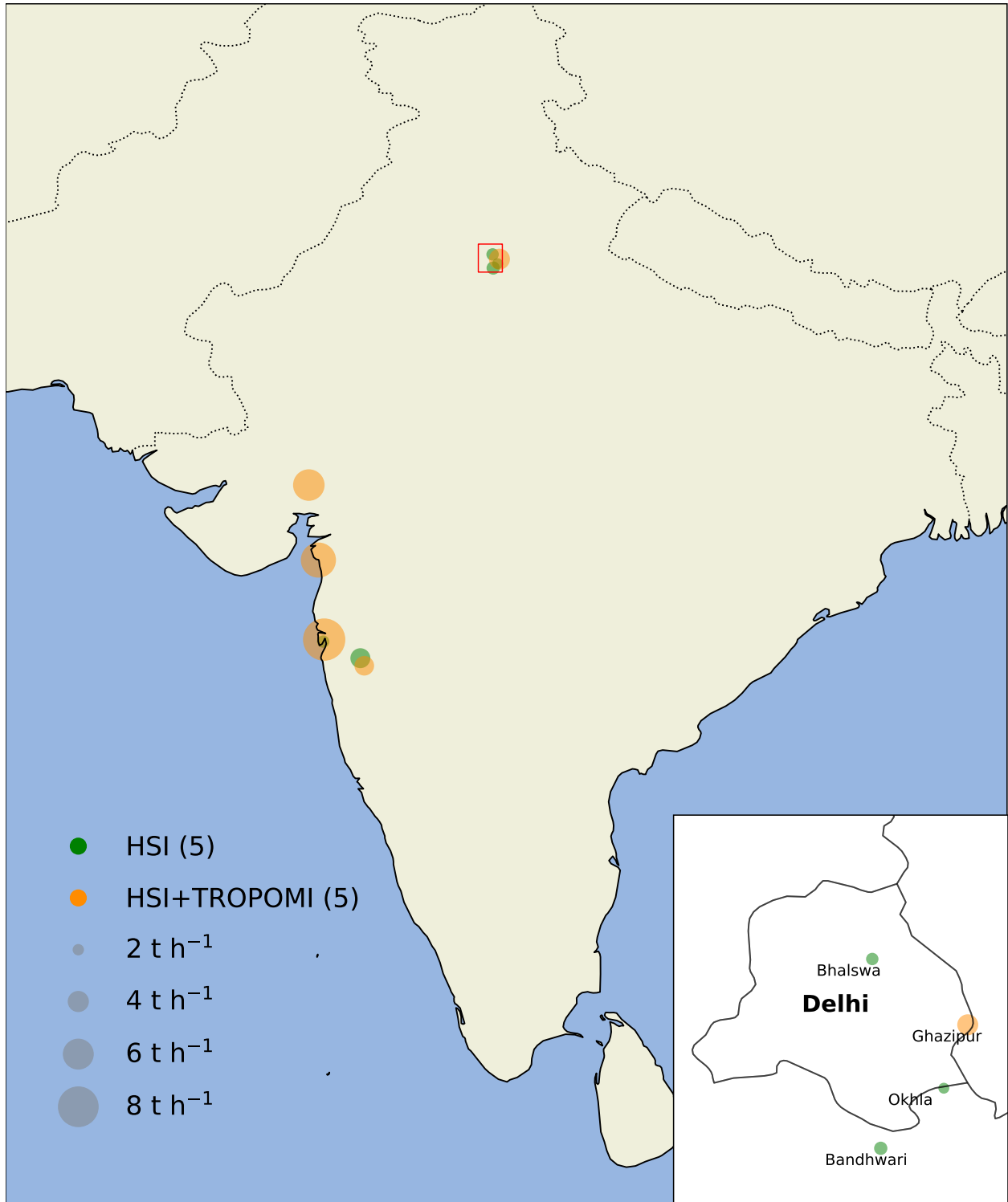


Figure S7: Landfill emissions detected by HSI across India, with a zoomed-in view of the Delhi region.

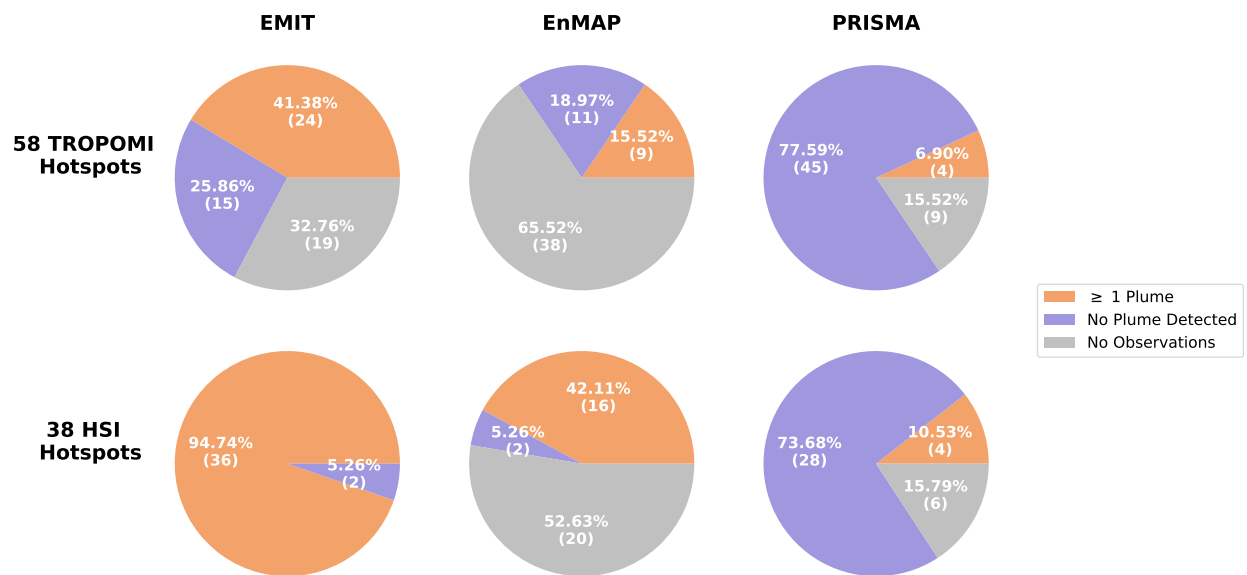


Figure S8: Variation in landfill hot spots detection efficiency by different HSIs (EMIT, EnMAP, and PRISMA) distinguishing three categories: detection of at least one plume (orange), clear-sky observations without detected plumes (purple), and no clear-sky observations (grey). Corresponding percentage values are displayed next to the number of hot spots in each category.

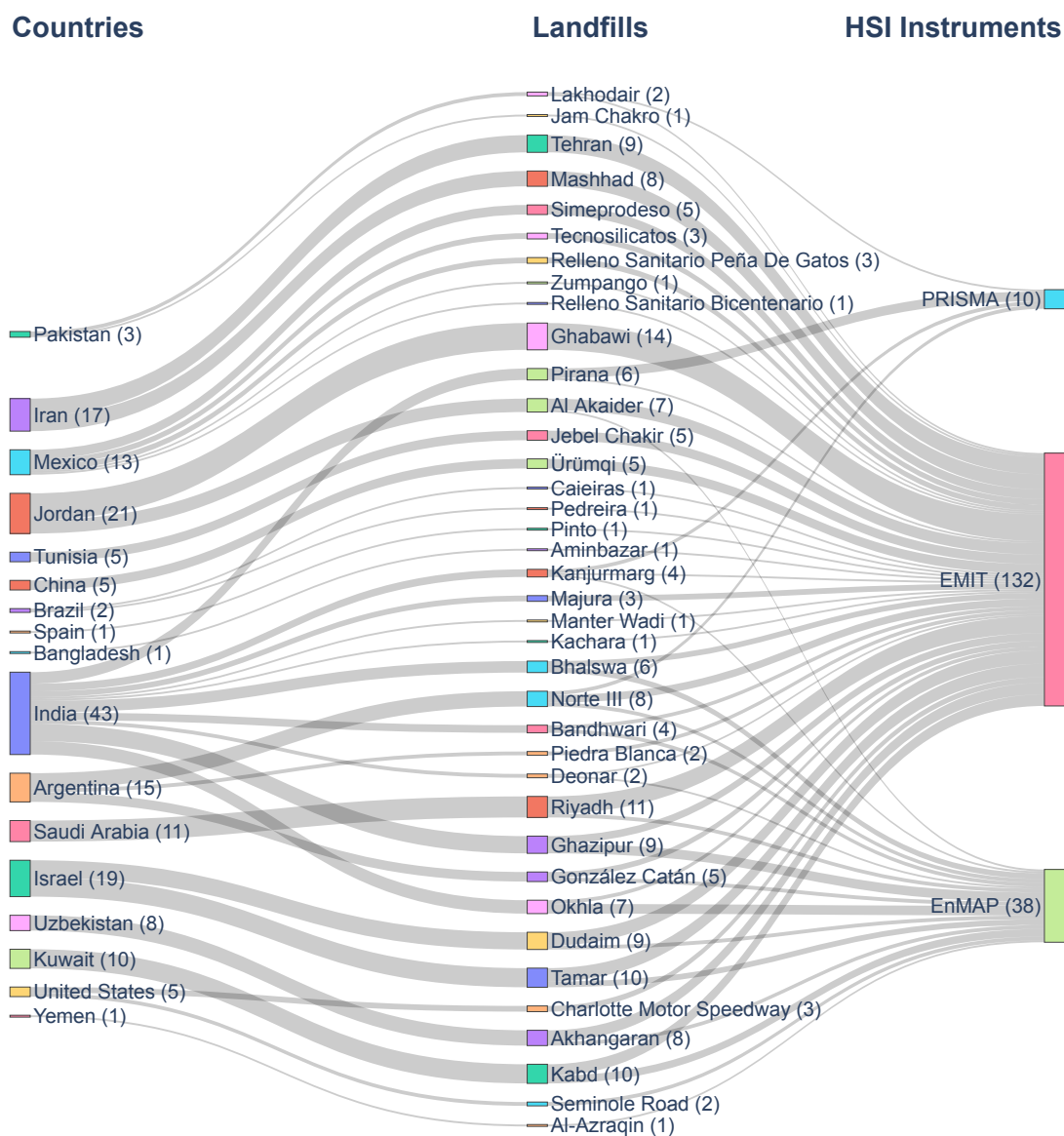


Figure S9: Sankey plot for the numbers of landfill plumes detected by HSIs (EMIT, EnMAP, and PRISMA). The numbers beside each country represent the total number of plumes detected from landfills within that country; the numbers next to each landfill indicate the number of detected plumes, and the numbers on the right show the total observations per HSI instrument.

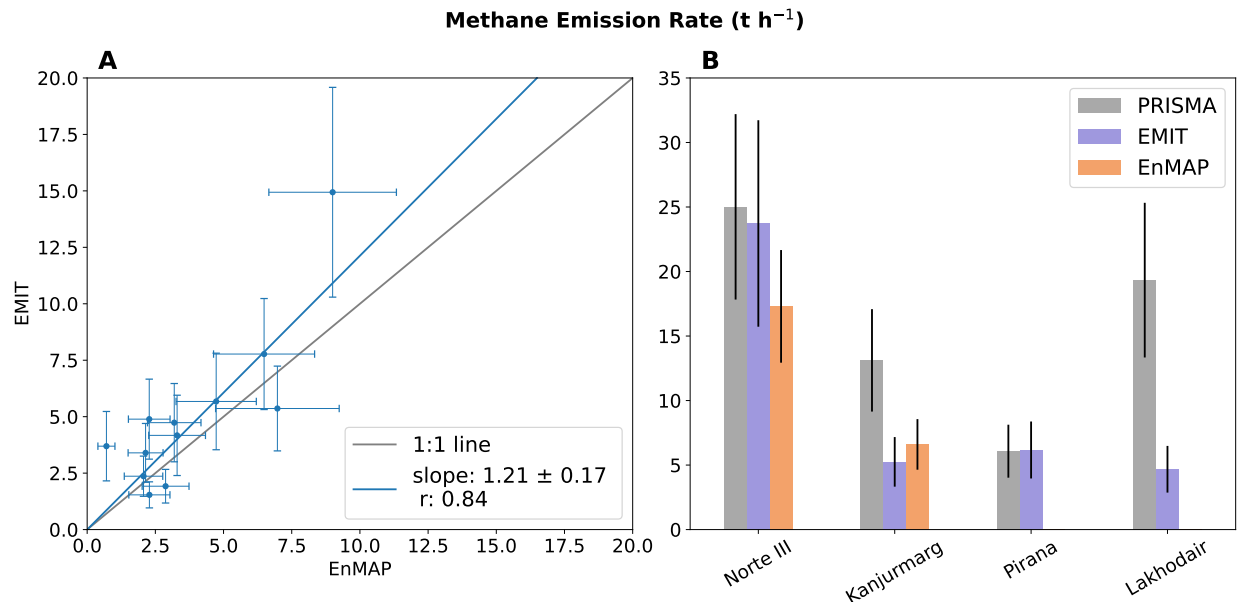


Figure S10: Comparison of average methane emission rates estimated with different HSIs for the same 24 landfill sites. (A) The orthogonal distance regression between methane emission rates estimated using the EMIT and EnMAP HSI sensors. (B) The methane emission rates of the four landfills with methane plumes detected by PRISMA. Observations were made by EMIT and EnMAP in 2023 for all sites. PRISMA observations were from 2023 for the Norte III and Pirana landfills, and 2020–2022 for the Kanjurmarg and Lakhodair landfills.

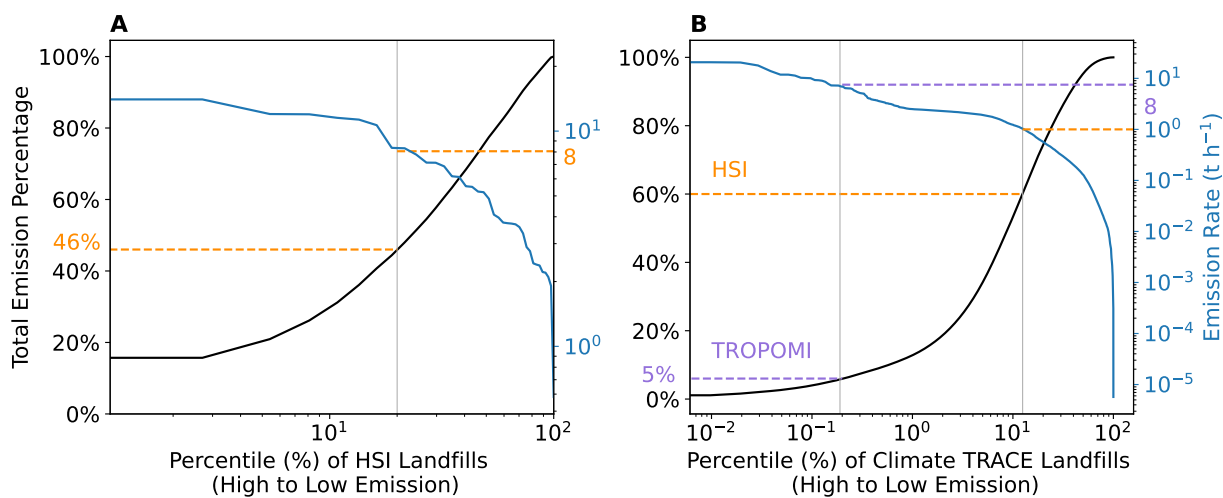


Figure S11: Cumulative distributions of landfill methane emissions. The black lines represent the cumulative distribution function of summed emission rates across landfill percentiles (in descending order), while the blue line indicates the emission rates at each respective percentile. (A) Landfills identified by HSIs. The top 20% of the highest emitting landfills emit 46% of total HIS-detected landfill emissions. (B) Landfills in the Climate TRACE dataset. The $1 t h^{-1}$ limit (orange line) and the $8 t h^{-1}$ limit (purple line) correspond to the estimated detection thresholds of HSI and TROPOMI, respectively.

Sentinel-2 Images (2023) of Climate TRACE Top 20 Landfills

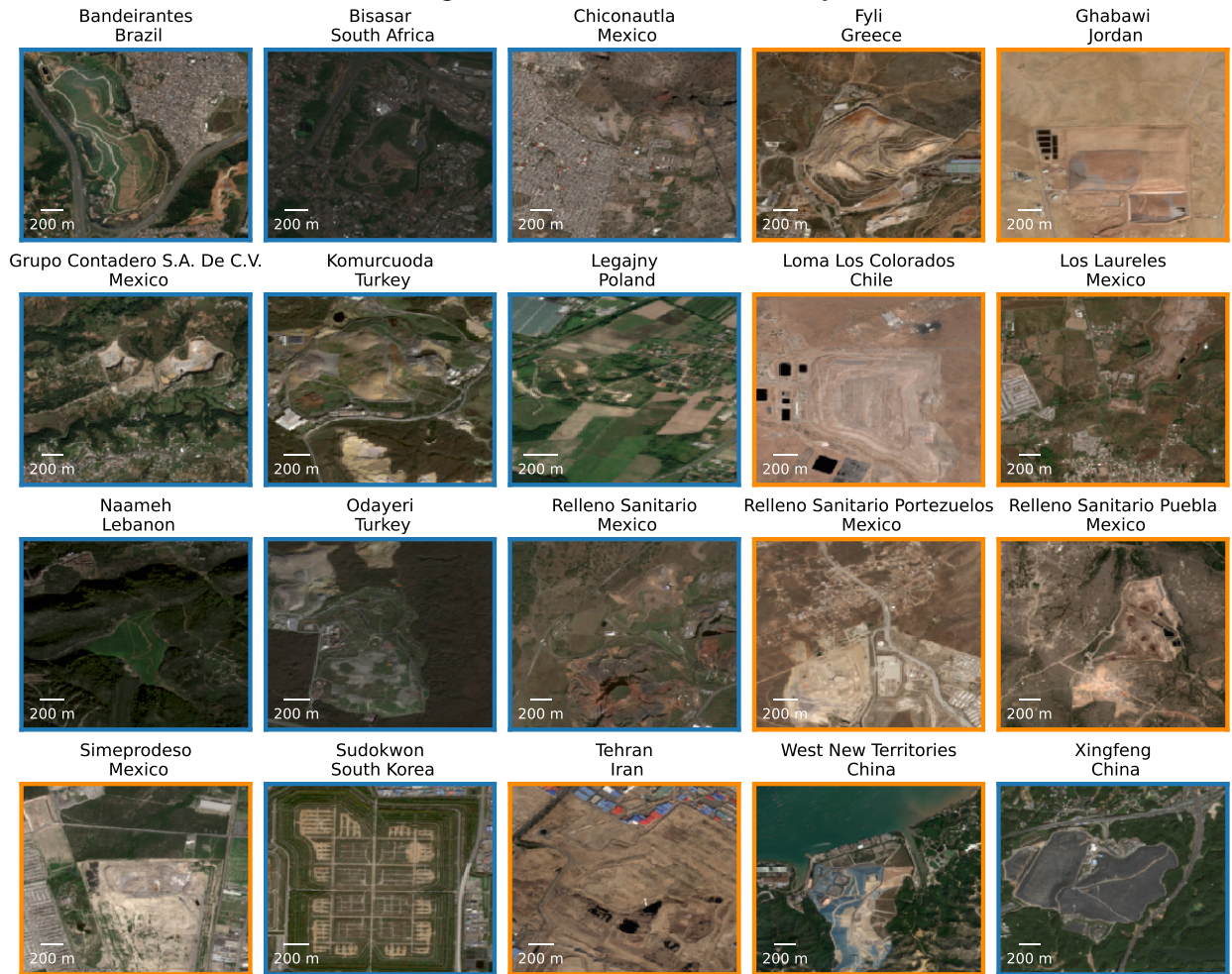


Figure S12: Sentinel-2 satellite images from 2023¹² showing the top 20 emitting landfills identified in the Climate TRACE dataset. An orange frame indicates that the HSIs detected methane plumes, while a blue frame means they did not.

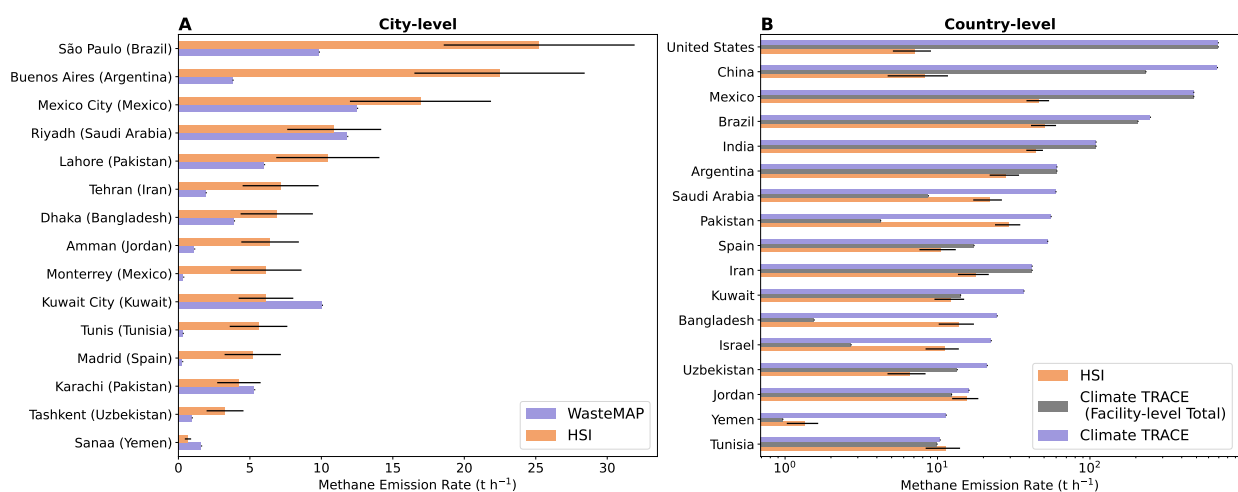


Figure S13: Comparison of methane emissions from landfills summed at the (A) city and (B) country levels, estimated using HSI observations, WasteMAP, and Climate TRACE inventories. The emission rates calculated using HSI represent the total emissions from measured and analyzed landfills in each city and country (Table S6 and S7). The total facility emissions for each country (not just the landfills analyzed using the HSI), as reported by Climate TRACE, are shown in gray.

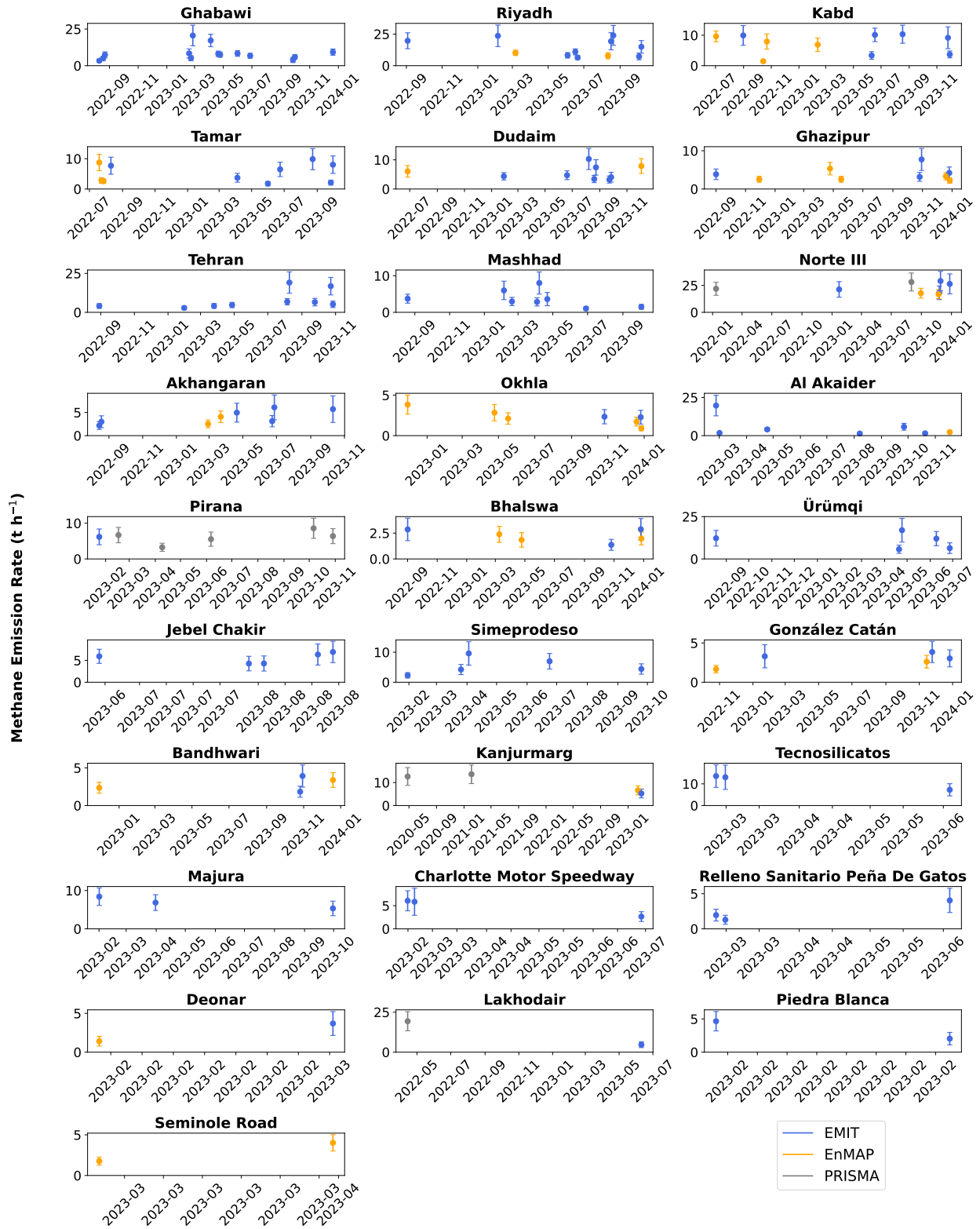


Figure S14: Time series of methane emission rates from landfills detected at least once with HSIs.

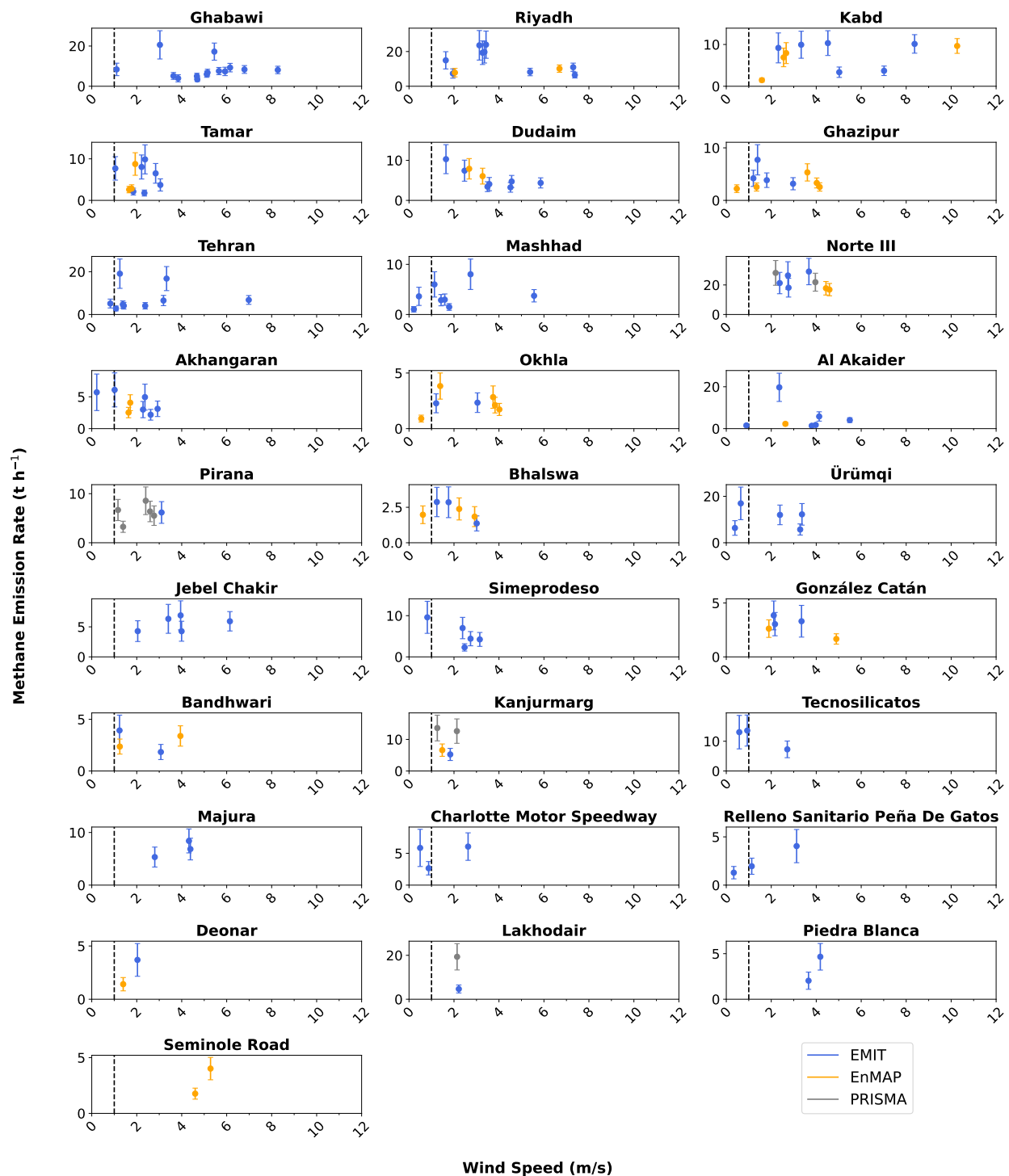


Figure S15: Relationship between wind speed and methane emission rates from landfills detected at least once with HSIs.

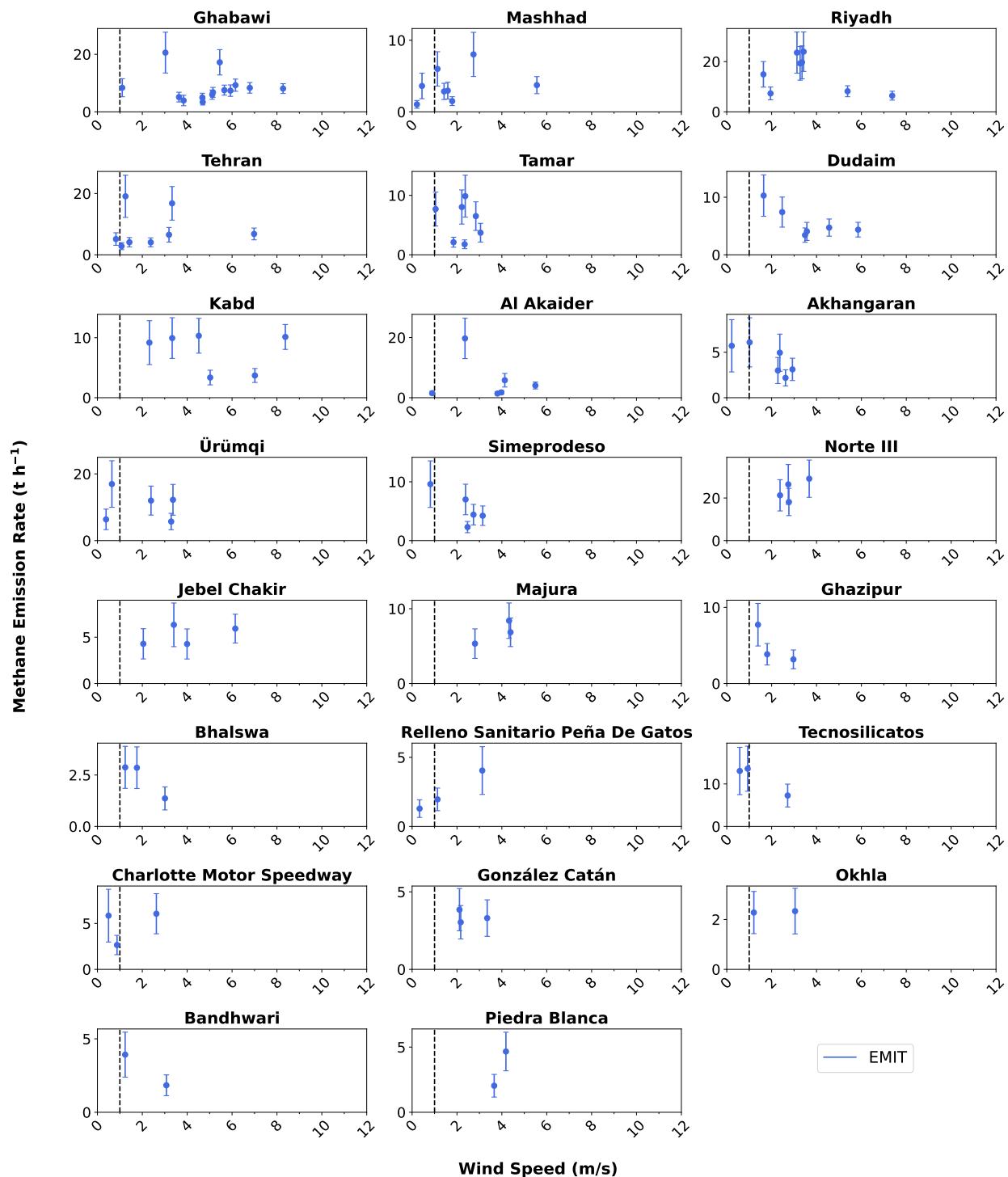


Figure S16: Same as Fig. S15, but showing emission estimates derived from EMIT data using the IME-fetch method.

Sentinel-2 Images (2023) of the Ghabawi Landfill (Jordan)

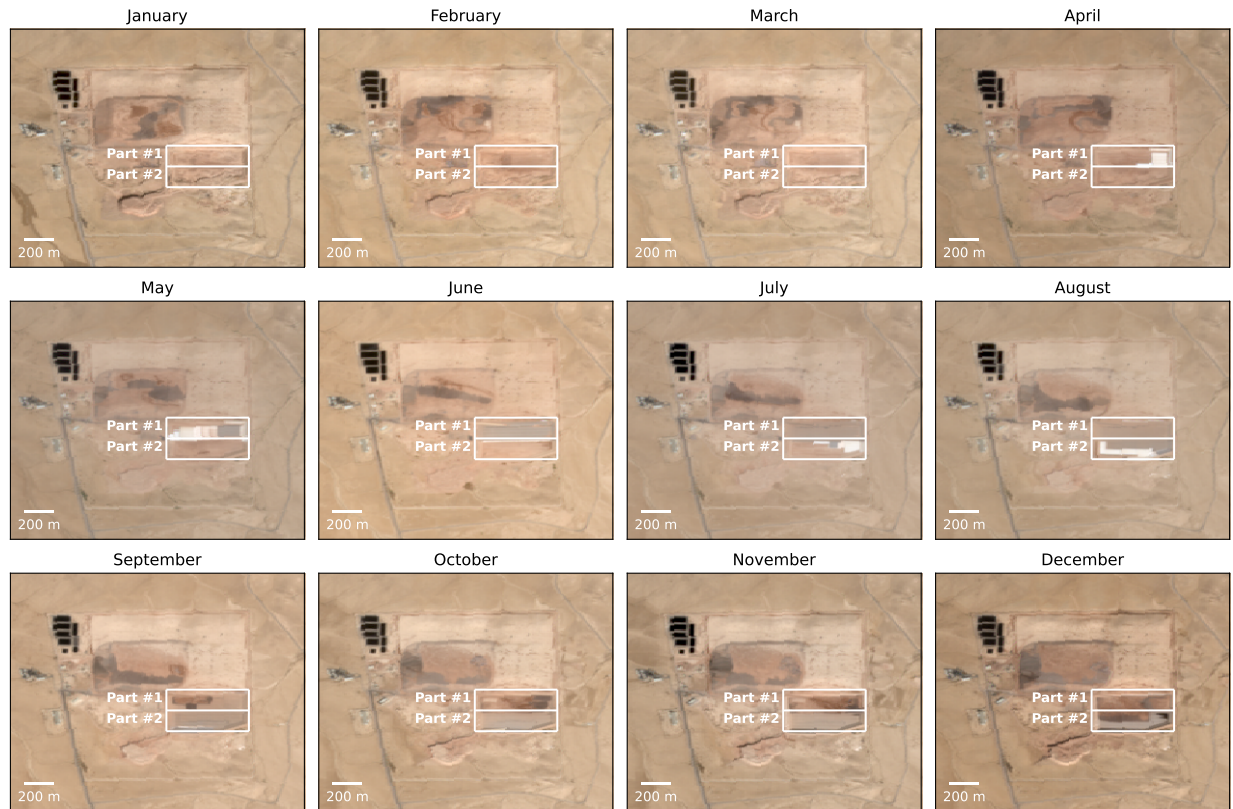


Figure S17: Monthly Sentinel-2 RGB images¹² captured in 2023 showing the Ghabawi Landfill in Jordan. The two white rectangles highlight two cells within the recently developed southern section. Movie S1 shows a time-lapse sequence of all cloud-free Sentinel-2 RGB images captured throughout 2023.

Sentinel-2 Images (2023) of the Ghazipur Landfill (India)

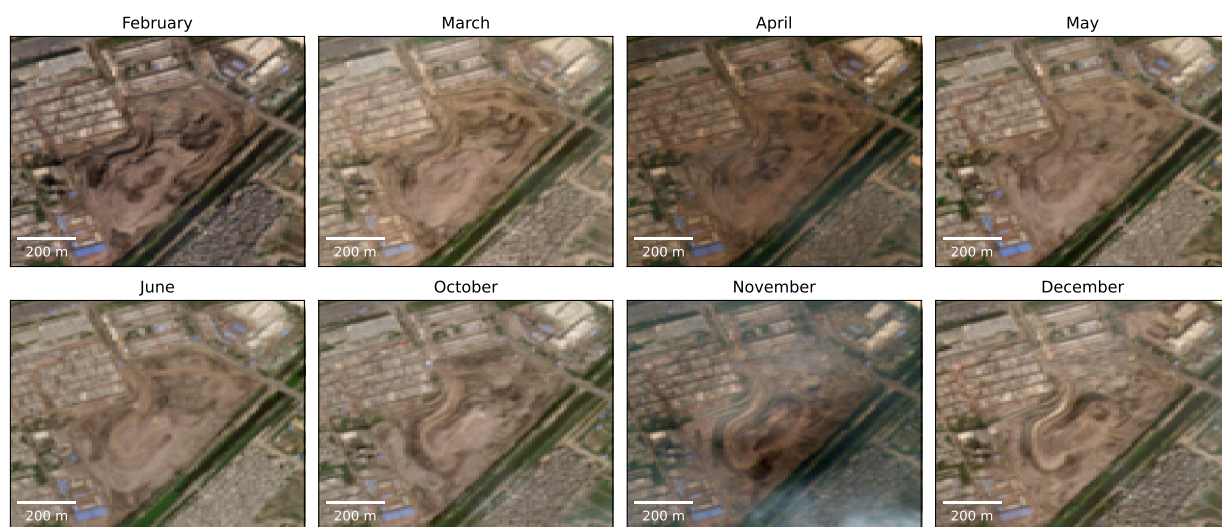


Figure S18: Monthly Sentinel-2 RGB images¹² captured in 2023 showing the Ghazipur Landfill in India. Movie S2 shows a time-lapse sequence of all cloud-free Sentinel-2 RGB images captured throughout 2023.

Table S1: Methane emission rates for HSI measured landfills.

Country	Landfill Name	Latitude	Longitude	Plume Counts	Null Detections	Emission ($t\ h^{-1}$)	Uncertainty (%)
Argentina	González Catán	-34.7849	-58.6665	5	-	2.8 ± 0.9	34.1
Argentina	Norte III	-34.5272	-58.6259	8	-	22.0 ± 6.4	29.2
Argentina	Piedra Blanca	-31.5198	-64.2354	2	-	3.3 ± 1.3	38.8
Bangladesh	Aminbazar	23.7979	90.2988	1	-	4.1 ± 1.6	39.8
Brazil	Caieiras	-23.3467	-46.772	1	-	14.0 ± 4.8	34.3
Brazil	Pedreira	-23.4037	-46.5608	1	-	11.5 ± 4.0	34.7
China	Ürümqi	44.0384	87.8651	5	-	10.7 ± 4.4	41.2
India	Bandhwari	28.4021	77.1717	4	1	2.4 ± 0.8	34.3
India	Bhalswa	28.7418	77.1565	6	-	2.2 ± 0.8	35.9
India	Deonar	19.0727	72.9285	2	1	2.2 ± 0.9	42.9
India	Ghazipur	28.6237	77.3277	9	-	4.0 ± 1.3	33.7
India	Kachara	18.6589	73.8558	1	-	3.8 ± 1.5	41.0
India	Kanjurmang	19.1233	72.952	4	-	8.3 ± 2.7	32.2
India	Majura	21.1089	72.8081	3	-	6.9 ± 2.1	30.9
India	Manter Wadi	18.4702	73.9537	1	-	3.7 ± 1.5	39.7
India	Okhla	28.5099	77.2849	7	1	1.9 ± 0.7	35.3
India	Pirana	22.9824	72.569	6	-	6.1 ± 2.1	34.8
Iran	Mashhad	36.2392	59.9882	8	-	3.7 ± 1.6	42.2
Iran	Tehran	35.4585	51.3302	9	-	7.8 ± 2.8	36.5
Israel	Dudaim	31.3217	34.7392	9	-	6.2 ± 2.1	33.7
Israel	Tamar	31.1329	35.2013	10	-	5.2 ± 1.8	34.4
Jordan	Al Akaidar	32.5143	36.1101	7	1	3.6 ± 1.3	34.9
Jordan	Ghabawi	31.9302	36.1888	14	-	8.4 ± 2.4	28.9
Kuwait	Kabd	29.1634	47.9138	10	-	7.1 ± 2.1	30.1
Mexico	Relleno Sanitario Bicentenario	19.6512	-99.2788	1	-	2.4 ± 1.0	40.6
Mexico	Relleno Sanitario Peña De Gatos	19.4031	-98.8422	3	-	2.4 ± 1.1	45.0
Mexico	Simeprodeso	25.8712	-100.2993	5	-	5.5 ± 2.2	39.0
Mexico	Tecnosilicatos	19.3241	-98.8033	3	-	11.3 ± 4.5	40.0
Mexico	Zumpango	19.7954	-99.01	1	-	2.1 ± 0.9	44.2
Pakistan	Jam Chakro	25.027	67.0359	1	-	5.2 ± 1.9	35.9
Pakistan	Lakhodair	31.6248	74.4176	2	-	12.0 ± 4.2	34.8
Saudi Arabia	Riyadh	24.6155	46.8953	11	-	12.0 ± 3.4	28.5
Spain	Pinto	40.2636	-3.6316	1	-	7.1 ± 2.5	35.0
Tunisia	Jebel Chakir	36.7371	10.0775	5	-	5.5 ± 2.0	35.9
United States	Charlotte Motor Speedway	35.3405	-80.6579	3	-	4.9 ± 2.0	41.8
United States	Seminole Road	33.6621	-84.257	2	-	2.9 ± 0.8	26.5
Uzbekistan	Akhanganar	41.0967	69.4838	8	-	3.7 ± 1.4	37.1
Yemen	Al-Azraqin	15.477	44.1545	1	1	0.6 ± 0.2	33.2

'Null Detections' refers to cases where EnMAP or EMIT has clear-sky overpasses but no plume is detected.

Table S2: Methane emission rates aggregated by country.

Country	Emission (t h ⁻¹)	Uncertainty (%)
Argentina	28.1 ± 6.6	23.6
Bangladesh	4.1 ± 1.6	39.8
Brazil	25.6 ± 6.3	24.5
China	10.7 ± 4.4	41.2
India	41.4 ± 5.0	12.1
Iran	11.5 ± 3.2	28.2
Israel	11.4 ± 2.7	24.1
Jordan	11.9 ± 2.7	22.8
Kuwait	7.1 ± 2.1	30.1
Mexico	23.7 ± 5.3	22.3
Pakistan	17.2 ± 4.6	26.6
Saudi Arabia	12.0 ± 3.4	28.5
Spain	7.1 ± 2.5	35.0
Tunisia	5.5 ± 2.0	35.9
United States	7.7 ± 2.2	28.0
Uzbekistan	3.7 ± 1.4	37.1
Yemen	0.6 ± 0.2	33.2

Total of HSI landfill emissions in Table S1 by country. The uncertainties on average emissions for individual landfills within a country are assumed to be independent and are combined in quadrature (square root of the sum of squared uncertainties) to obtain the overall uncertainty for that country.

Table S3: Comparison of landfill methane emission rates between HSI estimates and observational estimates (OBS) from previous studies.

Country	Landfill Name	Latitude	Longitude	HSI (t h ⁻¹)	OBS (t h ⁻¹)	HSI Year	OBS Report Year	OBS Source
Argentina	Norte III	-34.5291	-58.6222	22.0 ± 6.4	21.9 ± 7.8	2022, 2023	2021	GHGSat ³
India	Ghazipur	28.6238	77.3278	4.0 ± 1.3	1.6 ± 1.1	2022, 2023	2021	GHGSat ³
India	Kanjurmarg	19.1232	72.9535	8.3 ± 2.7	6.4 ± 4.0	2020, 2021, 2023	2021	GHGSat ³
Iran	Tehran	35.4587	51.33	7.1 ± 2.8	5.0 ± 1.0	2022, 2023	2022	EMIT ¹³
Pakistan	Lakhodair	31.6257	74.4179	12.0 ± 4.2	7.1 ± 3.1	2022, 2023	2020	GHGSat ³
Spain	Pinto	40.259	-3.6357	7.1 ± 2.5	6.6 ± 0.9	2023	2018	In-situ ¹⁴
United States	Charlotte Motor Speedway	35.3393	-80.6585	4.9 ± 2.0	2.9 ± 1.0	2023	2022	AVIRIS-NG ¹⁵
United States	Seminole Road	33.6623	-84.2577	2.9 ± 0.8	2.9 ± 1.1	2023	2022	ASU GAO ¹⁵

Table S4: Comparison of landfill methane emission rates between HSI and the Climate TRACE inventory.

Country	Landfill Name	HSI (t h ⁻¹)	Climate TRACE (t h ⁻¹)	Climate TRACE Report Source	Climate TRACE Report Year
Argentina	González Catán	2.8 ± 0.9	2.2	Waste Atlas	2013
Argentina	Norte III	22.0 ± 6.4	3.3	Waste Atlas	2013
Argentina	Piedra Blanca	3.3 ± 1.3	1.7	METER/OSM	2022
Bangladesh	Aminbazar	4.1 ± 1.6	1.5	METER/OSM	2022
India	Bandhwari	2.4 ± 0.8	0.02	Global Plastic Watch	2021
India	Bhalswa	2.2 ± 0.8	1.4	Waste Atlas	2013
India	Deonar	2.2 ± 0.9	2.4	Waste Atlas	2013
India	Ghazipur	4.0 ± 1.3	2.0	Waste Atlas	2013
India	Kachara	3.8 ± 1.5	0.3	Global Plastic Watch	2021
India	Kanjurmarg	8.3 ± 2.7	0.4	Global Plastic Watch	2021
India	Majura	6.9 ± 2.1	0.2	Global Plastic Watch	2021
India	Manter Wadi	3.7 ± 1.5	0.3	Global Plastic Watch	2021
India	Okhla	1.9 ± 0.7	1.9	METER/OSM	2022
India	Pirana	6.1 ± 2.1	2.2	Waste Atlas	2013
Iran	Tehran	7.8 ± 2.8	20.5	Waste Atlas	2013
Jordan	Al Akaidar	3.6 ± 1.3	1.6	Waste Atlas	2013
Jordan	Ghabawi	8.4 ± 2.4	7.3	Waste Atlas	2013
Kuwait	Kabd	7.1 ± 2.1	1.5	METER/OSM	2022
Mexico	Relleno Sanitario Bicentenario	2.4 ± 1.0	1.3	MEX INEGI	2016
Mexico	Simeprodeso	5.5 ± 2.2	17.9	MEX INEGI	2022
Pakistan	Jam Chakro	5.2 ± 1.9	2.0	Waste Atlas	2013
Saudi Arabia	Riyadh	12.0 ± 3.4	1.9	METER/OSM	2022
Spain	Pinto	7.1 ± 2.5	1.6	E-PRTR	2021
United States	Charlotte Motor Speedway	4.9 ± 2.0	0.7	EPA GHGRP	2021
United States	Seminole Road	2.9 ± 0.8	1.4	EPA GHGRP	2021
Yemen	Al-Azraqin	0.6 ± 0.2	1.0	METER/OSM	2022

Table S5: Comparison of HSI emission rates and observational estimates (OBS) from previous studies with Climate TRACE inventory for the top 20 highest emitting landfills from Climate TRACE.

Country	Landfill Name	Latitude	Longitude	Climate TRACE (t h ⁻¹)	HSI (t h ⁻¹)	OBS (t h ⁻¹)	OBS Source
Iran	Tehran	35.4585	51.3302	20.5	7.8 ± 2.8	5.0 ± 1.0	EMIT ¹³
Mexico	Simeprodeso	25.8712	-100.2993	17.9	5.5 ± 2.2	-	-
Chile	Loma Los Colorados	-32.957	-70.7962	11.8	10.7 ± 3.9	1.2 ± 0.3	AVIRIS-NG ¹⁵
Mexico	Los Laureles	20.5461	-103.1751	11.8	3.4 ± 1.4	-	-
Greece	Fyli	38.0748	23.6489	10.2	5.3 ± 2.6	-	-
Mexico	Relleno Sanitario	32.4073	-116.7459	9.3	6.9 ± 2.4	-	-
	Portezuelos					-	-
China	West New Territories	22.4193	113.9329	8.6	7.7 ± 2.7	-	-
Mexico	Relleno Sanitario	18.9827	-98.1368	7.8	1.7 ± 0.7	-	-
	Puebla					-	-
Jordan	Ghabawi	31.9302	36.1888	7.3	8.4 ± 2.4	-	-

Table S6: Comparison of landfill methane emission rates estimated using HSI and the city-level WasteMAP inventory.

Country	City	Landfills	WasteMAP (t h^{-1})	HSI (t h^{-1})	HSI WasteMAP
Argentina	Buenos Aires	Norte III (8), González Catán (5)	3.8	24.8 ± 6.5	6.5
Bangladesh	Dhaka	Aminbazar (1)	3.9	4.1 ± 1.6	1.1
Brazil	São Paulo	Caieiras (1), Pedreira (1)	9.8	25.6 ± 6.3	2.6
Iran	Tehran	Tehran (9)	1.9	7.8 ± 2.8	4.1
Jordan	Amman	Ghabawi (14)	1.1	8.4 ± 2.4	7.6
Kuwait	Kuwait City	Kabd (10)	10.0	7.1 ± 2.1	0.7
Mexico	Mexico City	Zumpango (1), Relleno Sanitario Peña De Gatos (3) Relleno Sanitario Bicentenario (1), Tecnosilicatos (3)	12.5	18.2 ± 4.8	1.5
Mexico	Monterrey	Sineprodeso (5)	0.3	5.5 ± 2.2	16.3
Pakistan	Lahore	Lakhodair (2)	6.0	12.0 ± 4.2	2.0
Pakistan	Karachi	Jam Chakro (1)	5.3	5.2 ± 1.9	1.0
Saudi Arabia	Riyadh	Riyadh (11)	11.8	12.0 ± 3.4	1.0
Spain	Madrid	Pinto (1)	0.3	7.1 ± 2.5	26.8
Tunisia	Tunis	Jebel Chakir (5)	0.3	5.5 ± 2.0	18.2
Uzbekistan	Tashkent	Akhangan (8)	0.9	3.7 ± 1.4	4.0
Yemen	Sanaa	Al-Azraqin (1)	1.6	0.6 ± 0.2	0.4

The HSI emission estimates account for the cumulative methane emissions from individual landfills within each city. There can be additional waste facilities within the city with emissions not observed by the HSI. The numbers in brackets following each landfill name represent the number of detected plumes.

Table S7: Comparison of landfill methane emission rates estimated using HSI and the country-level Climate TRACE inventory.

Country	Climate TRACE (t h^{-1})	HSI (t h^{-1})	$\frac{\text{HSI}}{\text{Climate TRACE}}$ (%)
Argentina	60.3	30.9 ± 6.7	51.3
Bangladesh	24.5	8.2 ± 2.3	33.4
Brazil	247.8	51.1 ± 8.8	20.6
China	681.5	10.7 ± 4.4	1.6
India	108.9	41.4 ± 5.0	38.0
Iran	41.5	19.3 ± 4.3	46.5
Israel	22.4	11.4 ± 2.7	50.8
Jordan	16.0	20.3 ± 3.6	127.0
Kuwait	36.7	14.3 ± 3.0	38.9
Mexico	476.6	47.4 ± 7.5	10.0
Pakistan	55.3	34.5 ± 6.5	62.4
Saudi Arabia	59.4	23.9 ± 4.8	40.3
Spain	52.5	14.3 ± 3.5	27.2
Tunisia	10.3	11.1 ± 2.8	107.2
United States	690.4	7.7 ± 2.2	1.1
Uzbekistan	21.1	7.5 ± 2.0	35.5
Yemen	11.3	1.2 ± 0.3	10.3

The HSI estimation accounts for the cumulative methane emissions from individual landfills within each country. There can be additional landfills within each country with emissions not observed by the HSI analysis presented here.

103 Movie S1. Time-series of Sentinel-2 RGB images in 2023 for the Ghabawi
104 landfill.

105 Movie S2. Time-series of Sentinel-2 RGB images in 2023 for the Ghazipur
106 landfill.

107 References

- 108 (1) Varon, D. J.; McKeever, J.; Jervis, D.; Maasackers, J. D.; Pandey, S.; Houweling, S.;
109 Aben, I.; Scarpelli, T.; Jacob, D. J. Satellite Discovery of Anomalously Large Methane
110 Point Sources From Oil/Gas Production. *Geophys. Res. Lett.* **2019**, *46*, 13507–13516.
- 111 (2) Varon, D. J.; Jacob, D. J.; Jervis, D.; McKeever, J. Quantifying Time-Averaged
112 Methane Emissions from Individual Coal Mine Vents with GHGSat-D Satellite Ob-
113 servations. *Environ. Sci. Technol.* **2020**, *54*, 10246–10253.
- 114 (3) Maasackers, J. D.; Varon, D. J.; Elfarsdóttir, A.; McKeever, J.; Jervis, D.; Mahapa-
115 tra, G.; Pandey, S.; Lorente, A.; Borsdorff, T.; Foorthuis, L. R.; Schuit, B. J.; Tol, P.;
116 van Kempen, T. A.; van Hees, R.; Aben, I. Using Satellites to Uncover Large Methane
117 Emissions from Landfills. *Sci. Adv.* **2022**, *8*, eabn9683.
- 118 (4) Varon, D. J.; Jacob, D. J.; McKeever, J.; Jervis, D.; Durak, B. O. A.; Xia, Y.; Huang, Y.
119 Quantifying Methane Point Sources from Fine-Scale Satellite Observations of Atmo-
120 spheric Methane Plumes. *Atmos. Meas. Tech.* **2018**, *11*, 5673–5686.
- 121 (5) Sherwin, E. D.; Rutherford, J. S.; Chen, Y.; Aminfard, S.; Kort, E. A.; Jackson, R. B.;
122 Brandt, A. R. Single-Blind Validation of Space-Based Point-Source Detection and
123 Quantification of Onshore Methane Emissions. *Sci. Rep.* **2023**, *13*, 3836.
- 124 (6) Sherwin, E. D.; El Abbadi, S. H.; Burdeau, P. M.; Zhang, Z.; Chen, Z.; Rutherford, J. S.;
125 Chen, Y.; Brandt, A. R. Single-Blind Test of Nine Methane-Sensing Satellite Systems
126 from Three Continents. *Atmos. Meas. Tech.* **2024**, *17*, 765–782.

- 127 (7) Esri; Maxar; Geographics, E.; the GIS User Community ESRI World Imagery.
128 https://services.arcgisonline.com/ArcGIS/rest/services/World_Imagery/MapServer,
129 2022.
- 130 (8) Heikenfeld, M.; Marinescu, P. J.; Christensen, M.; Watson-Parris, D.; Senf, F.; van den
131 Heever, S. C.; Stier, P. Tobac 1.2: Towards a Flexible Framework for Tracking and
132 Analysis of Clouds in Diverse Datasets. *Geosci. Model Dev.* **2019**, *12*, 4551–4570.
- 133 (9) Zhang, X.; van der A, R.; Ding, J.; Eskes, H.; van Geffen, J.; Yin, Y.; Anema, J.;
134 Vagasky, C.; L. Lapierre, J.; Kuang, X. Spaceborne Observations of Lightning NO₂ in
135 the Arctic. *Environ. Sci. Technol.* **2023**, *57*, 2322–2332.
- 136 (10) Jacob, D. J.; Turner, A. J.; Maasakkers, J. D.; Sheng, J.; Sun, K.; Liu, X.; Chance, K.;
137 Aben, I.; McKeever, J.; Frankenberg, C. Satellite Observations of Atmospheric Methane
138 and Their Value for Quantifying Methane Emissions. *Atmos. Chem. Phys.* **2016**, *16*,
139 14371–14396.
- 140 (11) MacLean, J.-P. W.; Girard, M.; Jervis, D.; Marshall, D.; McKeever, J.; Ramier, A.;
141 Strupler, M.; Tarrant, E.; Young, D. Offshore Methane Detection and Quantification
142 from Space Using Sun Glint Measurements with the GHGSat Constellation. *Atmos.*
143 *Meas. Tech.* **2024**, *17*, 863–874.
- 144 (12) Sentinel-2 Cloud-Optimized GeoTIFFs. [https://registry.opendata.aws/sentinel-2-l2a-](https://registry.opendata.aws/sentinel-2-l2a-cogs/)
145 [cogs/](https://registry.opendata.aws/sentinel-2-l2a-cogs/), 2024.
- 146 (13) Thorpe, A. K. et al. Attribution of Individual Methane and Carbon Dioxide Emission
147 Sources Using EMIT Observations from Space. *Sci. Adv.* **2023**, *9*, eadh2391.
- 148 (14) Tu, Q. et al. Quantification of CH₄ Emissions from Waste Disposal Sites near the City
149 of Madrid Using Ground- and Space-Based Observations of COCCON, TROPOMI and
150 IASI. *Atmos. Chem. Phys.* **2022**, *22*, 295–317.

151 (15) Carbon Mapper data Retrieved from <https://data.carbonmapper.org>. 2024.